



Tuning the activity of cobalt 2-hydroxyphosphonoacetates-derived electrocatalysts for water splitting and oxygen reduction: Insights into the local order by pair distribution function analysis

Álvaro Vélchez-Cózar^a, Rosario M.P. Colodrero^a, Montse Bazaga-García^a, David Marrero-López^b, Sayed M. El-refaei^{c,d}, Patrícia A. Russo^d, Nicola Pinna^d, Pascual Olivera-Pastor^a, Aurelio Cabeza^{a,*}

^a Universidad de Málaga, Departamento de Química Inorgánica, Cristalografía y Mineralogía, Campus Teatinos s/n, Málaga 29071, Spain

^b Universidad de Málaga, Departamento de Física Aplicada I, Campus Teatinos s/n, Málaga 29071, Spain

^c Max-Planck-Institut für Chemische Energiekonversion, Stiftstraße 34-36, 45470 Mülheim an der Ruhr, Germany

^d Institut für Chemie and IRIS Adlershof, Humboldt-Universität zu Berlin, 12489 Berlin, Germany

ARTICLE INFO

Keywords:

Cobalt phosphonates/pyrophosphates/
phosphides
Electrocatalysts
PDF analysis
OER/HER/ORR
Water splitting

ABSTRACT

Pyrophosphate- or phosphide-based iron/cobalt electrocatalysts were prepared from the metal (R,S)-2-hydroxyphosphonoacetates to evaluate the effects of metal composition, N-doping and P-enrichment on the electrocatalytic activity. Rietveld and Pair Distribution Function analysis were used to determine phase composition. Irrespectively of the amorphous or crystalline nature, all pyrolyzed solids transformed under OER operation into biphasic Fe/CoO(OH), composed of discrete clusters (size ≤ 20 Å). Carbon paper-supported Fe_{0.2}Co_{0.8}O(OH) electrocatalysts displayed the best OER performances (overpotentials of 270–279 mV at 10 mA·cm⁻²), attributable to the formation of highly active bimetallic intermediate species. For HER, increased concentration of o-CoP in phosphide-based electrocatalysts resulted in improved performance, up to an overpotential of 140 mV. Employed as anode in alkaline water splitting, amorphous Fe-doped cobalt pyrophosphate and phosphide-derived electrocatalysts showed a cell voltage of 1.58 V at 10 mA·cm⁻², with comparable stability to that of RuO₂ and requiring lower voltage demand at high current densities.

1. Introduction

Transition metal-based electrocatalysts have garnered considerable attention as potential alternative materials for commercial noble metal catalysts in electrochemical technologies for energy conversion and storage, such as fuel cells and water electrolyzers [1,2]. Among them, phosphorus-containing electrocatalysts, especially metal phosphides and phosphates, are particularly attractive owing to their widely tunable

compositions and properties [3,4]. Although some issues related to catalytic efficiency and low electronic conductivity await management, the potential of P-containing transition metal electrocatalysts is still promising as they are prone to tailoring by using different synthetic strategies. A prominent methodology starts from coordination polymer precursors, such as metal phosphonates (MPs), which upon pyrolysis in different conditions lead to electrocatalytically active metal phosphides and/or polyphosphates [5–7]. This approach offers several advantages,

Abbreviations: ADPs, atomic displacement parameters; BET, Brunauer–Emmett–Teller; CA, chronoamperometric; CP, carbon paper; CVs, cyclic voltammograms; DI, deionized water; d-PDF, differential pair distribution function analysis; ECSA, electrochemical surface area; EDX, energy-dispersive X-ray spectroscopy; EIS, electrochemical impedance spectroscopy; GCE, glassy carbon electrode; HAADF-STEM, high angle annular dark field scanning transmission electron microscopy; HER, hydrogen evolution reaction; HPAA, (R,S)-2-hydroxyphosphonoacetic acid; HRTEM, high-resolution transmission electron microscopy; ICP-OES, inductively coupled plasma optical emission spectrometry; LSVs, linear sweep voltammograms; LXRPD, laboratory X-ray powder diffraction; MPs, metal phosphonates; OER, oxygen evolution reaction; ORR, oxygen reduction reaction; PAA, phosphonoacetic acid; PDF, pair distribution function; RHE, reversible hydrogen electrode; RDE, rotating disk electrode; RRDE, rotating ring-disk electrode; SAL, secondary auxiliary ligand; SEM, scanning electron microscopy; SXRPD, synchrotron X-ray powder diffraction; TGA, thermogravimetric analysis; TMPs, transition metal phosphides; TOF, turnover frequency; XPS, X-ray photoelectron spectroscopy.

* Corresponding author.

E-mail address: aurelio@uma.es (A. Cabeza).

<https://doi.org/10.1016/j.apcatb.2023.122963>

Received 16 March 2023; Received in revised form 22 May 2023; Accepted 4 June 2023

Available online 5 June 2023

0926-3373/© 2023 The Author(s). Published by Elsevier B.V. This is an open access article under the CC BY-NC-ND license (<http://creativecommons.org/licenses/by-nc-nd/4.0/>).

such as: (i) affordable synthesis, (ii) variability in metal coordination that can be further modified using, e.g., secondary auxiliary ligands (SAL), (iii) homogeneous dispersion of metal sites and (iv) controllable incorporation of heteroatoms (N, S, etc.) with the organic ligand [8,9].

Transition metal phosphides (TMPs), especially cobalt and nickel phosphides (M_xP ; $M = Co, Ni$), are among the most promising catalysts for HER [10], where the metal:P molar ratio plays a crucial role in enhancing the electrochemical properties [11,12]. Although the OER and ORR performances of P-containing electrocatalysts are still modest compared with those of precious-metal-based electrocatalysts, several strategies have been developed to boost their efficiency, including metal [13–19], boron, and/or heteroatom doping [20,21], e.g. nitrogen from organic sources such as melamine, urea, or imidazole, which have proven to enhance their intrinsic activities by formation of N-doped carbon/TMP heterostructures upon pyrolysis [22,23] or by forming mixed nitride- and phosphide-based composites supported on heteroatom-doped carbon [24]. Metal polyphosphates are also deemed as attractive materials for water oxidation in neutral and alkaline medium [25,26], since the phosphate group may act as proton acceptor, stabilizer, and/or inducing distortions on the local metal geometry [26]. Doping iron polyphosphate, $Fe_5(PO_4)_4(OH) \cdot 3H_2O$, with Co^{2+} showed an efficient performance as bifunctional electrocatalyst for ORR and OER [27]. In general, the improvement of the intrinsic activity in phosphorous-containing electrocatalysts is facilitated through different synthesis strategies, such as designing dual-atom catalysts and/or modifying structural features (vacancies, increased active sites / surface area, etc.) [28,29].

Other reported strategies for optimizing the OER and HER activities include the formation of amorphous metal (oxy)hydroxides on Ni_5P_4 nanosheets, which promote high electronic interaction and synergistic effects for promoting the catalytic pathway [30]. Additionally, polycrystalline metal (oxy)hydroxides can be grown on Fe metal [31] or $NiFeP$ nanostructures [32], resulting in highly active and stable water splitting electrocatalysts. Carbon-integrated CoP nanowires/layered double hydroxides (LDHs) [33], FeP nanosheets-integrated CoP [34], nickel foam-supported bimetal phosphide ($CoP@Ni_2P$) or $Ir_{0.05}-Co_2P/-Co_2P_2O_7$ [35,36], and carbon-supported Cu-doped CoP nanoparticles [37] catalysts have been also successfully tested in both HER and OER processes.

In general, electrode materials are complex heterostructures in which amorphous and crystalline phases may coexist. In addition, the electrochemical processes may induce changes, such as crystalline-to-amorphous transitions, undetectable by conventional LXR, or even giving rise to a full chemical transformation as in the case of the OER [38–42]. In this context, pair distribution function (PDF) analysis may provide valuable structural information relative to the intermediate-range structures, such as local disorders and domain sizes [43,44]. Hence, PDF analysis may aid in the understanding of short-range order structures and tracking their evolution during the electrochemical processes, which in turn may be correlated with specific material functionalities [45]. So, a PDF study demonstrated the presence of Ni^{2+} in $FeOOH$ nanosheet-based catalyst [31]. Furthermore, differential PDF (d-PDF) analysis, which involves subtracting a reference PDF for a given material, allows differentiating samples before and after electrochemical test to track key structural changes influencing the properties of the catalysts [46–50].

Herein, we study thoroughly the heterostructure and electrocatalytic properties of several metal hydroxyphosphonoacetate-derived electrocatalysts toward the OER, HER, and ORR. MPs were prepared by combining transition metal salts (Fe^{2+} , Co^{2+}) with the HPAA ligand, and used as precursors of metal pyrophosphate- or phosphide-based electrocatalysts. In addition, a systematic study of the factors enhancing electrocatalytic performances was conducted by: (i) synthesizing bimetallic catalysts, (ii) using imidazole as SAL in the synthesis process or (iii) mixing the initial precursors with imidazole or phosphonoacetic acid as additional N or P sources, respectively. For establishing valuable

structure/electrochemical performance relationships, Rietveld and PDF analyses were performed to comprehensively characterize and monitor the evolution and stability of the electrocatalysts.

2. Experimental section

2.1. Reagents and chemicals

Iron (II) sulphate heptahydrate ($FeSO_4 \cdot 7H_2O$, $\geq 99\%$), cobalt (II) chloride hexahydrate ($CoCl_2 \cdot 6H_2O$, $\geq 98\%$), cobalt (II) nitrate hexahydrate ($Co(NO_3)_2 \cdot 6H_2O$, $\geq 98\%$), and imidazole ($C_3H_4N_2$, $\geq 99.5\%$) were purchased from Sigma-Aldrich. Potassium hydroxide (KOH, $\geq 85\%$) and sulfuric acid (H_2SO_4 , $\geq 98\%$) were obtained from VWR. (*R,S*)-2-hydroxyphosphonoacetic acid (HPAA, $H_2O_3PCH(OH)COOH$, 50 % v/v) was acquired from BioLab. Carbon black (Super P® Conductive, $> 99\%$), RuO_2 (99.9 %), and phosphonoacetic acid (PAA, $H_2O_3PCH_2COOH$, $\geq 98\%$) were supplied by Alfa Aesar. Deionized water (DI) was employed for all synthesis

2.2. Synthesis of metal phosphonates $Fe_xCo_{1-x}[HO_3PCH(OH)CO_2] \cdot 2H_2O$ ($0 < x < 1$) ($Fe_xCo_{1-x}HPA$)

All MPs were synthesized using the same synthetic procedure. For example, the **CoHPA** was synthesized using the following procedure. 2.38 g of $CoCl_2 \cdot 6H_2O$ (10 mmol) and 2.2 mL of HPAA solution (10 mmol) were added to 30 mL of DI and refluxed for 24 h. The solid was filtered, washed with DI, and dried at 60 °C in an oven. Bimetallic precursors were identically prepared but changing the metal molar ratios of the corresponding metal salts. Reaction yield: $\sim 70\%$ based on the metal salts.

2.3. Synthesis of imidazole-containing cobalt phosphonate, $Co_3[(HO_3PCHOHCO_2)_2(C_3H_3N_2)_2] \cdot 2H_2O$ (**CoHPAIm**)

0.278 g of imidazole (4 mmol) and 0.22 mL of HPAA solution (1 mmol) were dissolved in 10 mL of DI water. Then, 0.5 mmol of $Co(NO_3)_2 \cdot 6H_2O$ was slowly added until a homogeneous solution was obtained and the pH was adjusted to 7, with a 1 M NH_3 aqueous solution. The reaction was carried out in a Teflon-lined autoclave at 200 °C for 4 days. The resulting polycrystalline solid was prepared following the same procedure described above. Reaction yield (based on metal salt): $\sim 75\%$. Elemental analysis (weight %) for **CoHPAIm**, Calcd: C 18.33, H 2.46, N 8.55. Found: C 18.55, H 2.49, N 8.20.

2.4. Derivatization of the precursors

The as-prepared MPs were physically mixed with imidazole (Im) in different proportions (30:70, 50:50 and 70:30 wt/wt%), or phosphonoacetic acid (PAA), using PAA:MP molar ratios of 1:1 for $Fe_xCo_{1-x}HPA$, or 2:1 for **CoHPAIm**. The mixed samples were grounded for 15 min in an agate mortar prior to pyrolysis.

2.5. Pyrolysis of the precursors

MPs or derivatized samples (60 mg) were pyrolyzed inside a tubular furnace (Thermolyne® 21100) under controlled N_2 or 5 %- H_2 /Ar atmospheres ($40 mL \cdot min^{-1}$) at 500–1000 °C, with a heating/cooling rate of $5^\circ C \cdot min^{-1}$, and holding times of 2 h in N_2 , and 3 h (**CoHPAIm**) or 5 h ($Fe_xCo_{1-x}HPA$) in 5 %- H_2 /Ar.

2.6. X-ray diffraction characterization

Empyrean PANalytical (Cu $K_{\alpha 1,2}$) or D8 ADVANCED (Mo $K_{\alpha 1}$) diffractometers were utilized to collect the LXR patterns. The amorphous content of selected metal phosphide-based catalysts was determined through Rietveld analysis, employing 25 wt% of Cr_2O_3

(NIST 674b) as internal standard [51].

SXRPD data were acquired at BL04-MSPD beamline of ALBA synchrotron (Spain) [52]. The crystal structure of CoHPAIm was determined using a simulated annealing approach implemented in EXPO2014 [53], starting from a HPA ligand, two Co²⁺ ions, and an imidazole molecule as initial fragments. The water molecule was identified using a difference Fourier map, while the position of H atoms could not be determined. Rietveld method [54] was used for the refinement of the crystal structure using the program GSAS-II [55]. Soft constraints with a weight factor of 15 were applied to ensure reasonable geometries in terms of bond distances and angles. Isotropic ADPs were independently refined for each metal and P atoms, while another set of ADPs were refined for the remaining atoms.

For PDF analysis, a wavelength of 0.3257(1) Å (38 keV) was chosen. For each sample, the final dataset was obtained by merging four patterns, each one measured for 38 min from 1° to 130° (2θ). D-PDF analysis of post-chronoamperometry samples was carried out by subtracting the carbon paper PDF from that of the catalyst sample deposited on the CP. Both samples were enclosed in 1.0 mm diameter capillaries. Experimental PDF data were acquired using the PDFgetX3 software [56], utilizing three optimized values of Q_{max} : 27 Å⁻¹ for highly crystalline samples, 18 Å⁻¹ for semicrystalline/amorphous compounds, and 16 Å⁻¹ for post-chronoamperometry samples. PDF data were analysed using the program PDFgui [57]. Nickel was used as standard for the determination of the instrumental parameters Q_{damp} (0.003706 Å⁻¹) and Q_{broad} (0.0123706 Å⁻¹). Scale factors, unit cell parameters, ADPs, and delta2 parameters were optimized for all PDF analyses [58,59]. Atomic positions were optimized for Fe, Co and P atoms in crystalline Fe-doped cobalt pyrophosphate, and for Co and O atoms in cobalt (oxy) hydroxides.

2.7. Elemental, thermal and microstructural characterization

Elemental analyses (C, H, N) were conducted using a Perkin-Elmer 2400 analyzer. Thermal analysis data were measured by a TA instruments (SDT-Q600 analyzer), employing open platinum crucibles under a N₂ flow in the range of 25–1000 °C and a heating rate of 10 °C·min⁻¹. N₂ adsorption–desorption isotherms were measured using an ASAP 2020 Micromeritics instrument at –196 °C. ICP-OES analyses were performed on a Perkin-Elmer Optima 7300DV spectrophotometer. Raman spectra were measured on a NRS-5100 JASCO spectrometer, utilizing 532 nm (Nd:YAG laser) excitation line and an acquisition time of 10 s. XPS studies were carried out on a Physical Electronics ESCA 5701 spectrometer. SEM images was performed on a HeliosNanolab 650 FEI. HRTEM and HAADF-STEM-EDX were conducted using a F200X Talos FEI.

2.8. Electrochemical measurements

A VSP-128 BioLogic workstation was used for conducting the electrochemical tests on a three-electrode configuration. The glassy carbon rotating disk electrode (Metrohm, area: 0.196 cm²) was utilized as working electrode. A platinum rod served as counter electrode, and the Ag/AgCl was used as the reference electrode. For the preparation of the working electrode, 4 mg of catalysts and 1.3 mg of a superconductive carbon were dispersed by sonification in a 1:1 v/v mixture of ethanol/water (470 µL) and 30 µL of Nafion® (5 wt%) for 1 h. Subsequently, 5 µL of the catalyst ink was drop-coated onto the GCE surface and air-dried (final catalyst loading of ~0.20 mg·cm⁻²). For stability tests, the working electrodes were prepared with a catalyst loading of 1 mg·cm⁻² supported on a hydrophobic CP (1 × 1 cm², MGL370 AvCarb). For comparison purposes, measurements were also performed using 20 wt% Pt/C (HISPEC® 3000) and RuO₂ as working electrodes under identical conditions.

Current densities were normalized with respect to the electrode surface area. Additionally, the potentials (vs. Ag/AgCl) were

transformed to the reversible hydrogen electrode (RHE) scale using the Eq. (1) [60]:

$$E_{(RHE)} = E_{(Ag/AgCl)} + 0.205 + 0.059 \cdot pH \quad (1)$$

The corresponding gas (N₂ for OER and HER, or O₂ for ORR) was bubbled over the electrolyte before each measurement and maintained throughout the electrochemical tests to guarantee the gas saturation of the solution. In general, CVs were recorded at a scan rate of 20 mV·s⁻¹. Subsequently, LSVs were obtained at a scan rate of 10 mV·s⁻¹ for GCE measurements and at 5 mV·s⁻¹ for CP measurements. All CVs and LSVs were corrected for iR-compensation (95 %) to account for the ohmic/solution resistance. Stability measurements were analyzed through CA responses at a specific potential value.

For OER measurements, a 1.0 M KOH solution was employed with a RDE rotation speed of 1600 rpm. CVs and LSVs were performed within the potential range of 1.0 and 1.7 V. The OER overpotential was determined using Eq. (2) [60]:

$$\eta = E_{(RHE)} - 1.23 \quad (2)$$

HER measurements were conducted in a 0.5 M H₂SO₄ electrolyte. CV experiments were performed within the potential range of –0.5 and 0 V, while LSV curves were recorded from –0.8 V to 0 V with RDE rotation at 2000 rpm. The Tafel slopes for OER and HER were calculated using Eq. (3) [60]:

$$\eta = a + b \log j \quad (3)$$

where η represents the overpotential, b is the Tafel slope and j the current density, respectively. EIS measurements were performed at a specific potential with an AC amplitude of 5 mV over a frequency range of 100 kHz to 0.1 Hz. ECSA values of the materials was estimated based on the double-layer capacitance (C_{dl}) obtained from CVs with variable scan rates in the non-Faradaic potential region. By plotting the capacitive current at a specific potential against the scan rate, a linear curve was obtained, and the C_{dl} value was determined as half the slope of the fitted line [61]. The ECSA value was estimated using Eq. (4):

$$ECSA = C_{dl}/C_s \quad (4)$$

where C_s is assumed to be ~40 µF·cm⁻² in 1.0 M KOH solution [62].

TOF values can be calculated from Eq. (5):

$$TOF = i/4Q \quad (5)$$

where i represents the current intensity and Q is the charge under the baseline-corrected voltametric peak obtained by integration, assuming a faradaic efficiency of 100 % [63].

ORR measurements were performed in a 0.1 M KOH solution with the RDE rotation at 1600 rpm. CVs and LSVs were recorded within the potential range of 0.2–1.2 V. Tafel plots for ORR were calculated and derived from the kinetic current using the Koutecký-Levich Eqs. (6–8):

$$\frac{1}{i} = \frac{1}{i_L} + \frac{1}{i_K} = \frac{4I_d}{B\omega^{1/2}} + \frac{1}{i_K} \quad (6)$$

$$B = 0.62 n F A C_o (D_o)^{2/3} \nu^{-1/6} \quad (7)$$

$$i_K = \frac{i \times i_L}{i_L - i} \quad (8)$$

where i represents the measured current, i_L and i_K are the diffusion-limiting and kinetic currents, ω is the electrode rotation rate (rad·s⁻¹), F is the Faraday constant, A is the electrode area, C_o is the bulk concentration of O₂ in 0.1 M KOH (1.2·10⁻⁶ mol·cm⁻³), D_o is the diffusion coefficient of O₂ in 0.1 M KOH (1.9·10⁻⁵ cm²·s⁻¹) and ν is the kinematic viscosity of the electrolyte (1.09·10⁻² cm²·s⁻¹). For the determination of the transfer electron number (n) and the %HO₂ production for ORR, RRDE measurements were conducted using a GCE with a concentric platinum ring Eqs. (9–10):

$$n = \frac{4I_d}{I_d + I_r/N} \quad (9)$$

$$\%HO_2^- = \frac{200I_r}{(I_dN + I_r)} \quad (10)$$

where N is the current collection efficiency of the platinum ring (0.37), and I_d and I_r represent the disk and ring currents, respectively. To access the stability of the catalyst with and without the addition of methanol, CA measurements at 0.5 V were carried out.

2.9. Alkaline water splitting

The water splitting experiments were performed on a PGSTAT302N AUTOLAB electrochemical workstation with a two-electrode homemade electrochemical cell. The catalyst loading drop-coated onto the CP ($1 \times 1 \text{ cm}^2$, AvCarb MGL370) was $1.0 \text{ mg} \cdot \text{cm}^{-2}$ for all electrodes. CVs and LSVs were conducted in the range of 1.0–2.0 V, using the same scan rates as mentioned earlier for CP measurements, in 1.0 M KOH. The theoretical quantity of released gas was determined using Faraday's law (Eq. 11)

$$n(H_2, O_2) = \frac{i \cdot t}{Z \cdot F} \quad (11)$$

where $n(H_2, O_2)$, i , t , Z , and F are the number of moles, current intensity, time, number of electrons involved in the reaction ($Z = 4$ for O_2 ; $Z = 2$ for H_2), and the Faraday constant, respectively. The quantity of experimental gas generated was determined using the water displacement method, considering Dalton's law (Eq. 12) with an estimated water vapor pressure of 0.03 atm under ambient conditions:

$$P_{total} = P_{gas} + P_{H_2O} \quad (12)$$

Subsequently, the volume of gas produced in the water displacement experiments was estimated using Eq. (13):

$$P \cdot V = n \cdot R \cdot T \quad (13)$$

Here, V represents the volume of gas produced, R is the gas constant and T the temperature. The Faradaic efficiency of the oxygen production process was calculated using Eq. (14):

$$\text{Faradaic efficiency} = \frac{\text{experimental } \mu\text{mol of } O_2}{\text{theoretical } \mu\text{mol of } O_2} \times 100 \quad (14)$$

3. Results and discussion

3.1. Characterization of the as-synthesized electrocatalyst precursors

Layered isostructural monometallic and bimetallic hydroxyphosphonoacetate precursors, denoted $\text{Fe}_x\text{Co}_{1-x}\text{HPA}$ ($0 < x < 1$) (Fig. S1), were prepared as described elsewhere [64,65] and their chemical compositions are showed in Table S1. The bimetallic phosphonates exhibit features of solid solutions as evidenced by the congruent variations of their unit cell parameters, which were determined by Rietveld refinement (Table S2). To increase the P or N content of the final catalysts, selected metal hydroxyphosphonoacetate compounds were additionally combined with PAA or Im, respectively. The resulting precursors are denoted $\text{P-Fe}_x\text{Co}_{1-x}\text{HPA}$ and $\text{Im-Fe}_x\text{Co}_{1-x}\text{HPA}$, respectively.

Moreover, attempts to synthesize nitrogen heteroatom-containing cobalt phosphonates by using imidazole as a SAL allowed to isolate a new crystalline solid, CoHPAIm , with formula $\text{Co}_3[(\text{HO}_3\text{PCHOHCO}_2)_2(\text{C}_3\text{H}_3\text{N}_2)_2] \cdot 2 \text{H}_2\text{O}$. Its crystal structure was solved from SXRPD. The final structural data as well as the Rietveld plot can be found in Table S3 and Fig. S2 respectively. The asymmetric part of its unit cell contains two crystallographic independent Co atoms, one HPA ligand and one imidazolate ion ligand (Fig. S3). Co1 is octahedrally

coordinated by two chelating bidentate HPA, via the phosphonate atom O(4) and the oxygen atom O(7) of the carboxylate group, and two monodentate phosphonate O(3). Co2 is pentacoordinated through a chelating bidentate HPA, OH group (O2) and carboxylate O(6), one monodentate phosphonate O(5), one water molecule and one apical monodentate imidazolate (N4). The layer structure is formed by chains of negatively charged, phosphonate-bridged Co1 complexes, $[\text{Co}(\text{HO}_3\text{PCHOHCO}_2)_2]_n^{2-}$, extending along the c -axis. These chains are further interconnected through positively charged Co2 complexes, $[\text{Co}(\text{C}_3\text{H}_3\text{N}_2) \cdot \text{H}_2\text{O}]^+$. Packing of the layers occurs in the a -axis direction, with the imidazolate groups situated in the interlayer region in an interdigitated fashion and separated 4.9 \AA to each other. The layers are held together only by Van der Waals interactions.

3.2. Structural and morphologic analysis of pyrolyzed materials

$\text{Fe}_x\text{Co}_{1-x}\text{T-N}_2$ (T = pyrolysis temperature) materials were obtained by pyrolytic treatment of the $\text{Fe}_x\text{Co}_{1-x}\text{HPA}$ precursors under N_2 atmosphere at 500, 700, and 1000 °C and their compositions are summarized in Table S4. Thermal analysis of a representative precursor revealed that several stepwise solid-state transformations occur (Fig. S4) when the compounds are heated up to 1000 °C in N_2 . All the solids pyrolyzed at 500 °C were amorphous, while pyrolysis at 700 °C yielded semicrystalline metal pyrophosphates (Fig. S5). In addition, pyrolysis of monometallic iron precursors at 1000 °C led to mixed iron pyrophosphates/phosphates. Morphologically, the samples pyrolyzed at 500 °C consist of irregular micrometric agglomerates (Fig. S6), composed in turn of nanosized particles creating porous sponge-like microstructures (Fig. 1a). The progressive particle sintering upon increasing the pyrolysis temperature results in a significant decrease of BET surface areas (Fig. S7), ranging from $33.0 \text{ m}^2 \cdot \text{g}^{-1}$ ($\text{Fe}_{0.2}\text{Co}_{0.8}\text{@500-N}_2$) to $2.4 \text{ m}^2 \cdot \text{g}^{-1}$ ($\text{Fe}_{0.2}\text{Co}_{0.8}\text{@1000-N}_2$), in line with an increased crystallinity (Fig. S6). As observed by HRTEM (Fig. 1b), the spacings of the fringes for the sample $\text{Fe}_{0.2}\text{Co}_{0.8}\text{@700-N}_2$ correspond to the interplanar lattice distances between the (302) or (020) atomic planes, characteristic of monoclinic $\text{Co}_2\text{P}_2\text{O}_7$ (PDF 01-084-2126). Regardless of particle size and crystallinity degree, HAADF-EDX mapping reveals a homogeneous elemental (Fe, Co, P, and O) distribution inside the particles for all studied pyrophosphate-based materials.

The synchrotron PDF patterns for selected materials are displayed in Fig. 2. As illustrated for $\text{Fe}_{0.2}\text{Co}_{0.8}\text{@500-N}_2$, amorphous cobalt pyrophosphates exhibit a very low degree of atomic order, which is consistent with a material composed of nanoclusters with undetected interatomic distances beyond 7 \AA . In contrast, $\text{Fe}_{0.2}\text{Co}_{0.8}\text{@700-N}_2$ maintains structural correlations over a wider range of r distances (Fig. 2a). The PDF pattern, refined in both the low ($1.4\text{--}10 \text{ \AA}$) and the intermediate ($10\text{--}50 \text{ \AA}$) r -ranges (Fig. 2b), is adequately fitted with the crystal structure of $m\text{-Co}_2\text{P}_2\text{O}_7$. The final values for the unit cells and ADP parameters are given in Table S5. The relatively good agreement factors in the low and intermediate r -ranges, $R_w = 22.44 \%$ and 17.50% , respectively, indicates that the aforementioned $m\text{-Co}_2\text{P}_2\text{O}_7$ is present in material $\text{Fe}_{0.2}\text{Co}_{0.8}\text{@700-N}_2$ and denotes the formation of a solid solution, coexisting with a little or nothing of other amorphous non-carbonaceous phases. At first glance, the atomic arrangements in amorphous (500 °C) and semicrystalline metal pyrophosphate (700 °C) solids are similar in the low r -range (Fig. 2c) since the peak positions for the former roughly match with those corresponding to individual atom-atom distance contributions in the refined local structure of $\text{Fe}_{0.2}\text{Co}_{0.8}\text{@700-N}_2$ (Fig. 2c).

Pyrolysis of the MP precursors in $5 \text{ \%H}_2/\text{Ar}$, at $750\text{--}850 \text{ }^\circ\text{C}$, led to essentially metal phosphide-based materials, denoted $\text{Fe}_x\text{Co}_{1-x}\text{T-N}_2$ (T = pyrolysis temperature). Rietveld phase quantifications and elemental analysis of the obtained compounds are shown in Table S6. Monometallic cobalt catalysts led to a mixture of the orthorhombic phases Co_2P (PDF 00-032-0306) and CoP (PDF 01-089-4862), while formation of iron phosphides from the corresponding monometallic

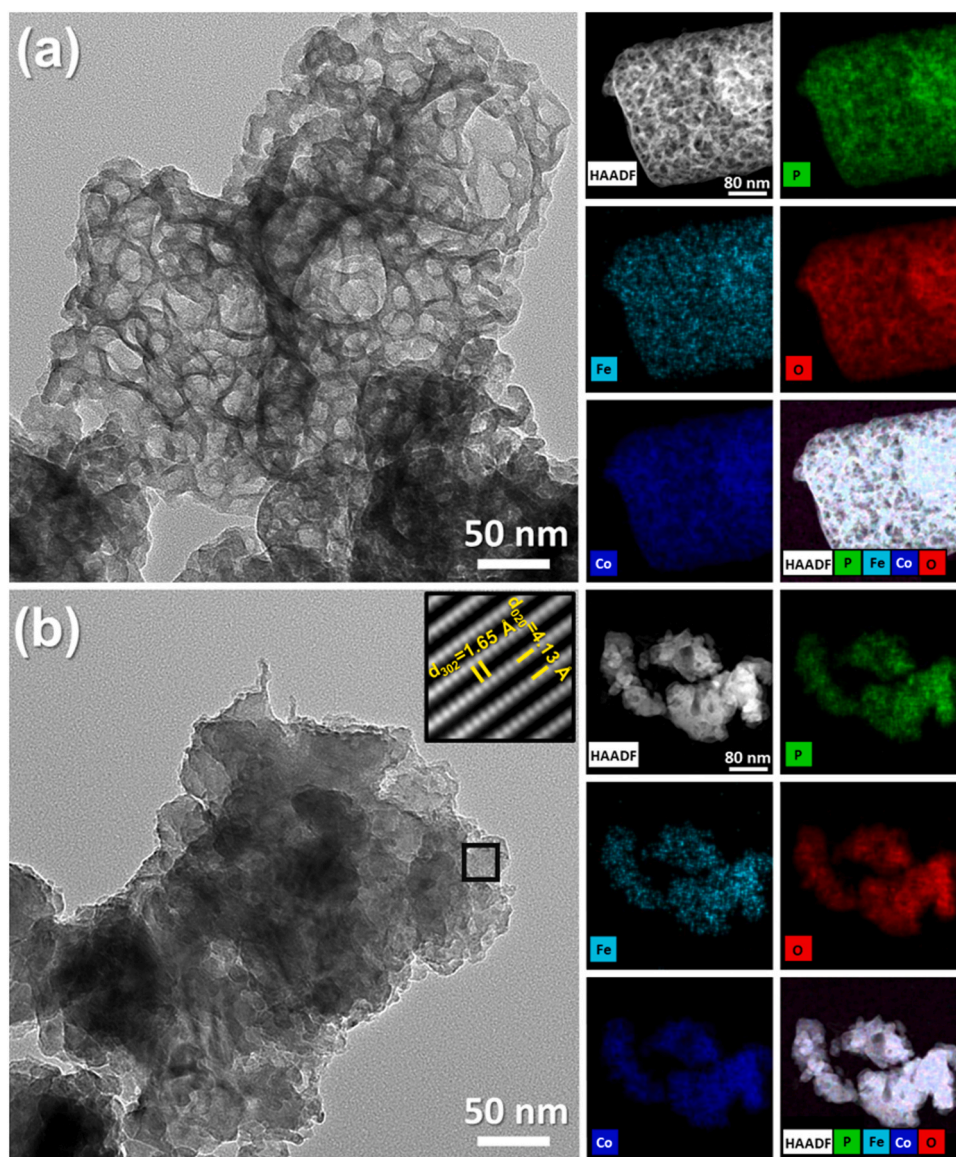


Fig. 1. HRTEM and HAADF-EDX images for (a) $\text{Fe}_{0.2}\text{Co}_{0.8}@ 500\text{-N}_2$ and (b) $\text{Fe}_{0.2}\text{Co}_{0.8}@ 700\text{-N}_2$ electrocatalysts (inside: Fourier transform pattern) highlighting the elemental distributions: Fe, Co, P, and O.

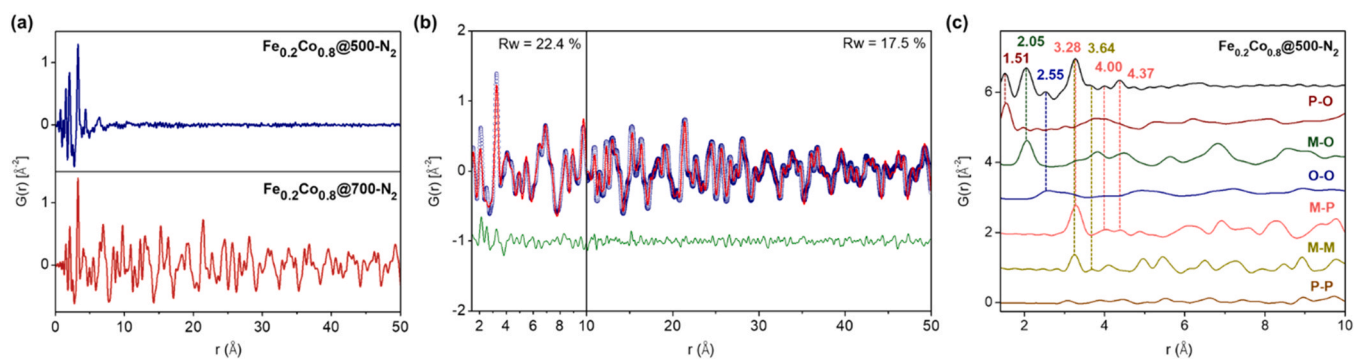


Fig. 2. (a) Comparison between the experimental PDF patterns of $\text{Fe}_{0.2}\text{Co}_{0.8}@ 500\text{-N}_2$ and $\text{Fe}_{0.2}\text{Co}_{0.8}@ 700\text{-N}_2$. (b) Experimental (blue circles) and fitted (red solid line) PDF patterns for $\text{Fe}_{0.2}\text{Co}_{0.8}@ 700\text{-N}_2$ in the low and high r -regions (difference curve is shown as a green solid line). (c) Experimental PDF pattern for $\text{Fe}_{0.2}\text{Co}_{0.8}@ 500\text{-N}_2$ with the individual interatomic distances obtained from the refined local structure of $\text{Fe}_{0.2}\text{Co}_{0.8}@ 700\text{-N}_2$.

precursor was incomplete, even at a pyrolysis temperature of 850 °C. On the other hand, bimetallic Fe/Co precursors promoted the formation of metal phosphide-based solid solutions, isostructural with the *o*-Co₂P and/or *o*-CoP phases. These results are comparable with those obtained by PDF analysis, in both, the low and intermediate *r*-ranges (Fig. S8 and Table S7). In the case of Co@ 800-H₂ and Fe_{0.2}Co_{0.8}@ 800-H₂, the PDF fits reveal that these solids are composed of the crystalline phases *o*-Co₂P (66.5–74.8 wt%) and *o*-CoP (33.5–25.2 wt%), without additional contributions associated with non-carbonaceous amorphous phases, as evidenced by the *R_w* parameter.

Aiming at improving the electrocatalytic performance of metal phosphide-based catalysts, modifications in catalyst preparation were brought about by using additional N and P sources [66], leading to variations in carbonaceous content and composition of the crystalline phases (Tables S6 and S7). Thus, as determined by Rietveld (Table S6) and PDF analyses (Fig. S9), pyrolysis of the Co²⁺-precursors in presence of PAA caused an increase in the percentage of the P-rich cobalt phosphide phase, *o*-CoP (≥ 90 wt%). For the solid solution P-Fe_{0.2}Co_{0.8}@ 800-H₂, the content of the phase *o*-CoP was slightly lower (83.7 wt%) than for the monometallic cobalt derivative (97.2 wt

%). The amorphous quantification, determined by Rietveld refinement (not showed), revealed that Co@ 800-H₂ contained 8.1 wt% of amorphous fraction, including the carbon residue. For the case of derivatized electrocatalysts P-Co@ 800-H₂ and Im-Co@ 800-H₂, the high amorphous content of 24.1 and 22.7 wt%, respectively, is attributable not only to the carbonaceous fraction (Table S6), but also to the presence of amorphous metal phosphides, as no other phases could be identified by PDF analysis. Nevertheless, the XPS spectra of cobalt phosphide catalysts reveal the formation of a thin oxidized superficial coverage surrounding the metal phosphide particles [67,68]. These spectra show Co 2p_{3/2} contributions of Co-O-P bonds (782.2 and 784.9 eV) and P 2p signals of P-O (133.9 eV) bonds, together with those attributable to Co-P (778.8 eV) and P-Co (129.8 and 130.9 eV) in metal phosphide environments (Fig. S10). Since the P 2p signals are compatible with P atom exhibiting a charge close to − 1 [69], the valence state of Co should be close to + 1. In addition, the Co-P peak at 778.8 eV, which is shifted to higher binding energy compared to the Co metal peak (777.9 eV), is in accordance with cobalt carrying a partial positive charge [70].

For the N-containing catalysts, XPS indicates that N is incorporated into the carbon matrix as pyrrolic, pyridinic and graphitic nitrogen

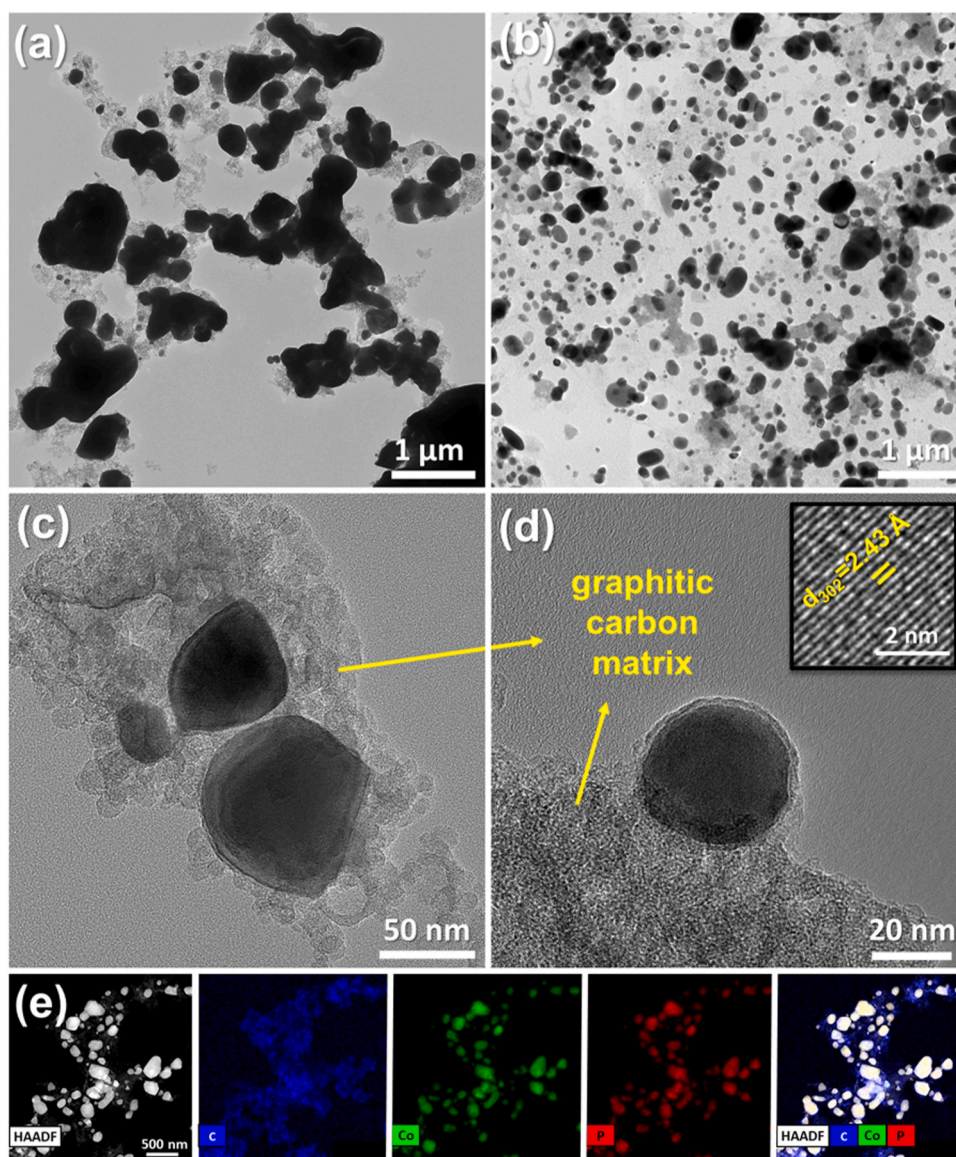


Fig. 3. Comparison of TEM images corresponding to the electrocatalysts (a) Co@ 800-H₂ and (b) P-Co@ 800-H₂. (c, d) HRTEM images of P-Co@ 800-H₂. (e) HAADF-EDX images of P-Co@ 800-H₂ highlighting the elemental distributions: C, Co and P.

species (Fig. S11) [71], with more than 50 % corresponding to the pyrrolic form. Furthermore, premixing precursors with PAA resulted in a considerable decrease in particle size (Fig. 3a,b), from 150 to 370 nm in **Co@ 800-H₂** to 80 nm in **P-Co@ 800-H₂**, as well as an increment in the carbonaceous content (Table S6) which embeds the metal phosphide particles (Fig. 3c,d). The spacing of the fringes observed in HRTEM is characteristic of the (302) atomic plane of *o*-CoP phase. On the other hand, the inclusion of imidazole as SAL in cobalt precursors (**CoHPAIm**) favored the formation of monophasic *o*-Co₂P catalyst at a temperature as low as 650 °C (Table S6). As revealed for **P-Co@ 800-H₂** (Fig. 3e), HAADF-EDX mapping suggests a homogeneous distribution of the elements within the particles. In addition, the Raman spectra in the carbon-region shows two bands, D and G (1350 and 1588 cm⁻¹, respectively), attributed to graphitic-based materials (Fig. S12) [72]. The intensity ratio of D/G (~ 1) suggests that the carbon coating is disordered [72].

3.3. Electrochemical performance

3.3.1. Oxygen evolution reaction

The OER activity of the pyrolyzed derivatives is summarized in Fig. S13 and their overpotential (η_{10}) values are given in Tables S4 and S6. For comparison purposes, the RuO₂ benchmark electrocatalyst is also included. It must be stressed that under the tested conditions of OER (1.0 M KOH), all pyrolyzed materials transformed into the electrocatalytic active cobalt (oxy)hydroxide phases, CoO(OH). So, when immersed **Fe_{0.2}Co_{0.8}@ 500-N₂** in 1 M KOH for 24 h (**Fe_{0.2}Co_{0.8}@500-N₂-KOH**), this solid transformed into a crystalline phase corresponding to the polymorph *R*-3m of CoO(OH) (Fig. S14). This was further confirmed by HAADF-EDX analysis, that indicates a very low phosphorous content (< 1 %). On the other hand, conversion of cobalt phosphide to CoO(OH) has been described in other studies [11,73].

It was noted that the electrochemical activity of cobalt-based catalysts follows a specific order according to the material source: crystalline metal pyrophosphate < amorphous metal pyrophosphate < crystalline P-enriched metal phosphide. Among the metal pyrophosphate-derived

catalysts, the best performance was achieved for the bimetallic material **Fe_{0.2}Co_{0.8}@ 500-N₂**, which exhibits an η_{10} value of 298 mV, when compared with the monometallic **Co@ 500-N₂** (355 mV).

While the amorphous pyrophosphate-based materials may be expected to be more reactive than their crystalline counterparts to transform into the active CoO(OH) catalyst, the fact that phosphide-based materials led to the most active OER catalysts deserves a further study. **Fe_xCo_{1-x}@ 800-H₂**, consisting mainly of *o*-Co₂P phase, showed the maximum OER activity for a composition $x = 0.2$ ($\eta_{10} = 324$ mV) (Fig. S13 and Table S6). This OER performance could be even improved by increasing the P content of the catalyst. So, the material **P-Fe_{0.2}Co_{0.8}@ 800-H₂**, mainly composed of *o*-CoP (83.7 wt%), displayed the lowest η_{10} value (280 mV) surpassing significantly to that of **Co@ 800-H₂** (361 mV) and the reference electrocatalyst RuO₂ (306 mV) (Fig. 4a). Additionally, **P-Fe_{0.2}Co_{0.8}@ 800-H₂** also achieves the fastest reaction kinetics (30.2 mV·dec⁻¹), which is slightly faster than that of the amorphous **Fe_{0.2}Co_{0.8}@ 500-N₂** (34.5 mV·dec⁻¹) (Fig. 4b). These Tafel slopes are indicative of a four-electron transfer process in which the rate-determining step is the transfer reaction of the third electron [74]. Overall, the electrochemical activity of **P-Fe_{0.2}Co_{0.8}@ 800-H₂** and **Fe_{0.2}Co_{0.8}@ 500-N₂** ranks among the most active metal phosphonate-derived OER electrocatalysts in alkaline conditions (Table S8).

To enlighten the OER process, the charge-transport kinetics were determined by EIS (Fig. 4c). The EIS curves show a depressed semicircle with similar values of solution resistance $R_s \sim 5 \Omega$, regardless of the electrocatalyst used (Table S9). The electrode response of EIS data was fitted by using two serial R-CPE elements. The high frequency process is attributed to surface porosity of the catalyst (R_p); while the low frequency process is typically associated with the charge-transfer resistance (R_{ct}) [75]. The R_p values are comparable for the different electrocatalyst, ranging from 1 to 3 Ω , indicating that differences in OER activity are due to different R_{ct} values. In particular, **P-Fe_{0.2}Co_{0.8}@ 800-H₂** exhibits the lowest R_{ct} value (5.3 Ω). For more in-depth information about the intrinsic properties of these electrocatalysts, an ECSA analysis was conducted (Fig. S15). Generally, higher

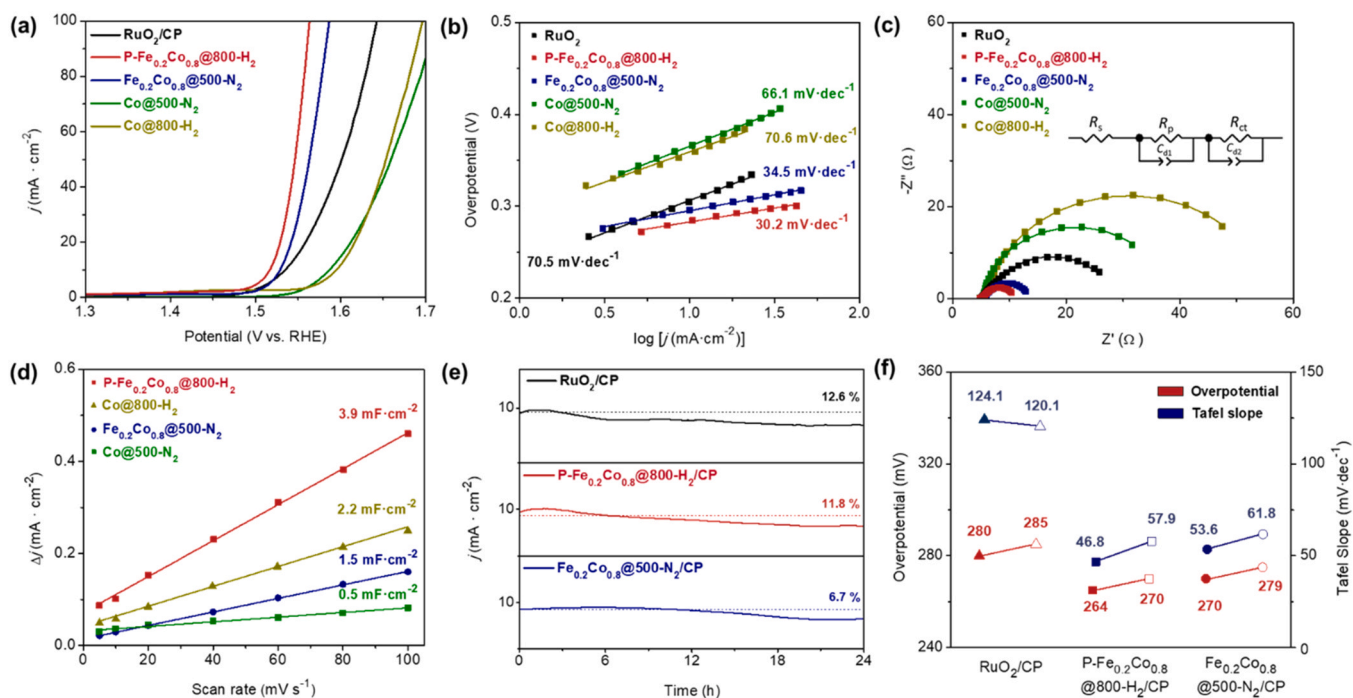


Fig. 4. OER data for selected electrocatalysts in 1.0 M KOH: (a) LSV curves; (b) Tafel plots; (c) EIS spectra at 300 mV (the inset shows the equivalent circuit model); (d) electrochemical double layer capacitances at 0.95 V; (e) long-term CA response at corresponding overpotential; and (f) evolution of the overpotential and Tafel slope values before (filled icons) and after (empty icons) CA stability tests for carbon paper-supported catalysts.

ECSA values are indicative of greater number of active sites in an electrocatalyst. Fe-doping in cobalt catalysts produces a considerable increase in C_{dl} , and consequently higher ECSA values (Fig. 4d). Thus, both **P-Fe_{0.2}Co_{0.8}@ 800-H₂** (29.6 m²·g⁻¹) and **Fe_{0.2}Co_{0.8}@ 500-N₂** (18.1 m²·g⁻¹) showed 1.5–2-fold ECSA values as compared with their monometallic counterparts. The ECSA values can be also correlated with particle characteristics, thus **P-Fe_{0.2}Co_{0.8}@ 800-H₂** with smaller particle size [76] and less agglomeration [77] (Fig. S16) show a larger active surface area than that of **Fe_{0.2}Co_{0.8}@ 500-N₂**, upon conversion to CoO (OH). On the other hand, the R_{ct} values for the metal pyrophosphate-derived increase in the order **Fe_{0.2}Co_{0.8}@ 500-N₂** (6.9 Ω) < **Fe_{0.2}Co_{0.8}@ 700-N₂** (176.8 Ω) < **Fe_{0.2}Co_{0.8}@ 1000-N₂** (498.9 Ω), suggesting that lowering the reaction resistance is correlated with an increased surface area, in accordance with ECSA analysis (Fig. S17) [78]. For this series of pyrophosphate-based catalysts, the calculated TOF values, used for estimating the OER intrinsic activity, were around 0.10 s⁻¹, which is significantly lower than that of **P-Fe_{0.2}Co_{0.8}@ 800-H₂** (0.28 s⁻¹, at η_{10} of 280 mV). These differences suggest that the relatively high apparent activity of **P-Fe_{0.2}Co_{0.8}@ 800-H₂** does not arise only from the higher ECSA but is also the result of more active catalytic sites on this catalyst, possibly due to electronic modulation effects from the combination of Fe and Co [79].

The electrochemical stability of the most active electrocatalysts is compared with that of commercial RuO₂ in Fig. 4e. As observed, the activity of **Fe_{0.2}Co_{0.8}@ 500-N₂/CP** remains the most stable, with a decay after 24 h of the current density of only 6.7 %, compared to those of **P-Fe_{0.2}Co_{0.8}@ 800-H₂/CP** and RuO₂/CP (11.8 % and 12.6 %, respectively). Nevertheless, LSV curves show that **P-Fe_{0.2}Co_{0.8}@ 800-H₂/CP** (270 mV) still achieves the lowest η_{10} value, slightly better than that of **Fe_{0.2}Co_{0.8}@ 500-N₂/CP** (279 mV) and RuO₂/CP (285 mV), and with remarkable kinetics for a 24-hour CA test (Figs. 4f and S18).

Post-reaction d-PDF analysis of **Fe_{0.2}Co_{0.8}@ 500-N₂** and **P-Fe_{0.2}Co_{0.8}@ 800-H₂** are shown in Fig. 5a. As observed, the peaks diminish quickly with the increasing r , indicating the formation of nanocrystalline CoO(OH) with a smaller domain size for the metal phosphide-derived catalyst (size \sim 20 Å). Significantly, the pre-immersed semicrystalline solid in KOH, **Fe_{0.2}Co_{0.8}@ 500-N₂-KOH**, exhibiting larger particle size (Fig. S19), displayed a much higher η_{10} value (334 mV) (Fig. S20). Differently to that previously observed for cobalt catalyst film formed in borate or phosphate electrolytes [44,80], the small clusters resulting from **Fe_{0.2}Co_{0.8}@ 500-N₂** and **P-Fe_{0.2}Co_{0.8}@ 800-H₂** fit better to a mixture of CoO(OH) polymorphs, *R-3m* and *P6₃/mmc*, which could be identified by using the software structureMining (Fig. 5b) [81]. The corresponding d-PDF analysis is shown in Fig. 5c. Fitting only could be carried out in the region 1.6–8 Å owing to disorder in the layer/cluster stacking. The final values for unit cells and ADP parameters are given in Table S10. The polymorph

composition in both types of catalysts was similar, which show enlarged *c*-axis for the *R-3m* polymorph, in comparison with the crystalline CoO (OH) compound. This variation in the *c* parameter could be related with the presence of adsorbed phosphate groups [44]. The presence of phosphorous as a minor component was revealed by HAADF-EDX (Fig. S21) analysis and P 2p XPS spectra (Fig. S22). HAADF-EDX analysis also indicates the presence of iron homogeneously distributed in the catalyst particles. The signal in the Co 2p_{3/2} region, at 780.7 eV, is compatible with an oxygen environment surrounding Co³⁺ ions [82,83].

Regarding to the active site characteristics, recent *operando* XAS and Raman, combined with RRDE studies have demonstrated the existence of structural reconstructions upon conversion of Fe-doped cobalt phosphides to the corresponding mixed metal (oxy)hydroxide, in which highly active oxo-bridged Co⁴⁺ and Co⁴⁺/Fe⁴⁺ intermediate species are formed. That is not the case when the bimetallic (oxy)hydroxide is directly used. Thus, the bimetallic catalysts derived from metal phosphide exhibit much higher OER activity [84]. Since our results are in accordance with those previously reported, we assume that a similar structural reconstruction occurs for the electrocatalysts prepared in this work, at least for those phosphide-based materials.

3.3.2. Hydrogen evolution reaction

For the monometallic cobalt catalyst, the performance is sustained at \sim 200 mV, even at pyrolysis temperatures as low as 650 °C upon N-doping if N is incorporated as SAL (Fig. S23 and Table S6). Indeed, **Co@ 800-H₂**, composed of a mixture of *o*-Co₂P and *o*-CoP, exhibit a η_{10} value of 208 mV, although N-doping did not significantly modify the performance of the catalysts (199 mV for the **CoIm@750-H₂** catalyst). Moreover, doping the cobalt derivatives with Fe had no beneficial effect on the activity compared with **Co@ 800-H₂**. The increase in the Fe-content led to an enrichment of *o*-Co₂P, α -Fe₂P₂O₇ and/or mixed Fe_xP phases at the expense of the most active phase, *o*-CoP, giving rise to a significant decay in activity [73,85,86].

Since P-rich TMP phases have been reported to lead to more active HER electrocatalysts [85,87], the effect of adding an extra P source (as PAA) has been evaluated. As expected, the η_{10} values decreased for both cobalt-based phosphides, from 208 to 140 mV, for **P-Co@ 800-H₂**, and from 199 to 165 mV for **P-CoIm@ 750-H₂** (Fig. 6a and Table S6), which can be explained by a pyrolytic transformation exclusively to the most active phase, *o*-CoP \geq 91 wt%.

Tafel slope values (Fig. 6b) vary in the range of 70–80 mV·dec⁻¹, indicating a HER mechanism controlled by the Volmer-Heyrovský route [88]. The EIS data for selected catalysts (Fig. 6c and Table S9) reveal similar solution resistance (R_s) and charge transfer resistance (R_p), but different R_{ct} values. **P-Co@ 800-H₂** exhibits the lowest total resistances ($R_t = R_p + R_{ct}$) indicating faster proton discharge kinetics. In addition, the ECSA value for this catalyst experienced a 1.5-fold increase (Fig. 6d

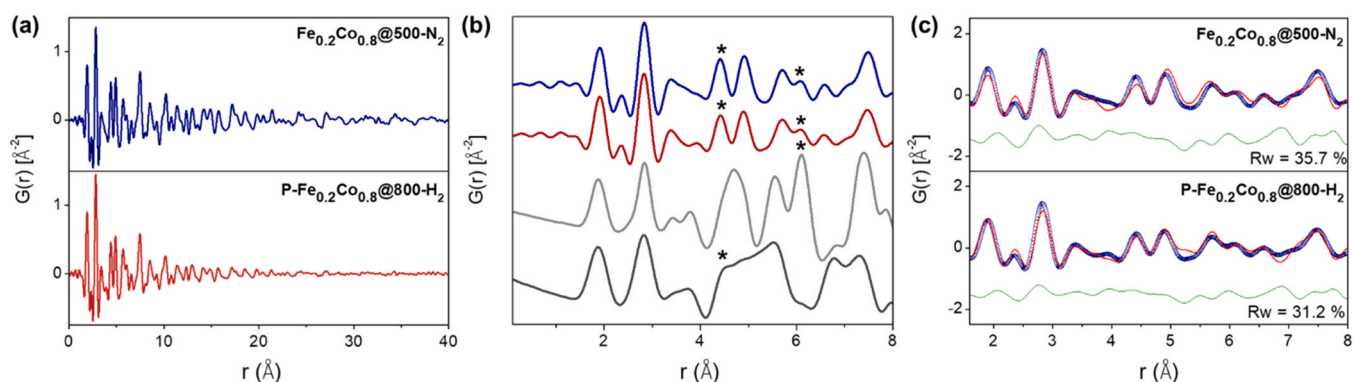


Fig. 5. Post-OER synchrotron PDF patterns: (a) experimental carbon-subtracted patterns of **Fe_{0.2}Co_{0.8}@ 500-N₂** (blue) and **P-Fe_{0.2}Co_{0.8}@ 800-H₂** (red). (b) Comparison of the PDF patterns with those calculated for *R-3m* (gray) and *P6₃/mmc* (black) CoO(OH) polymorphs in the low r region (*characteristic contributions of polymorphs), and (c) d-PDF fits including both polymorphs.

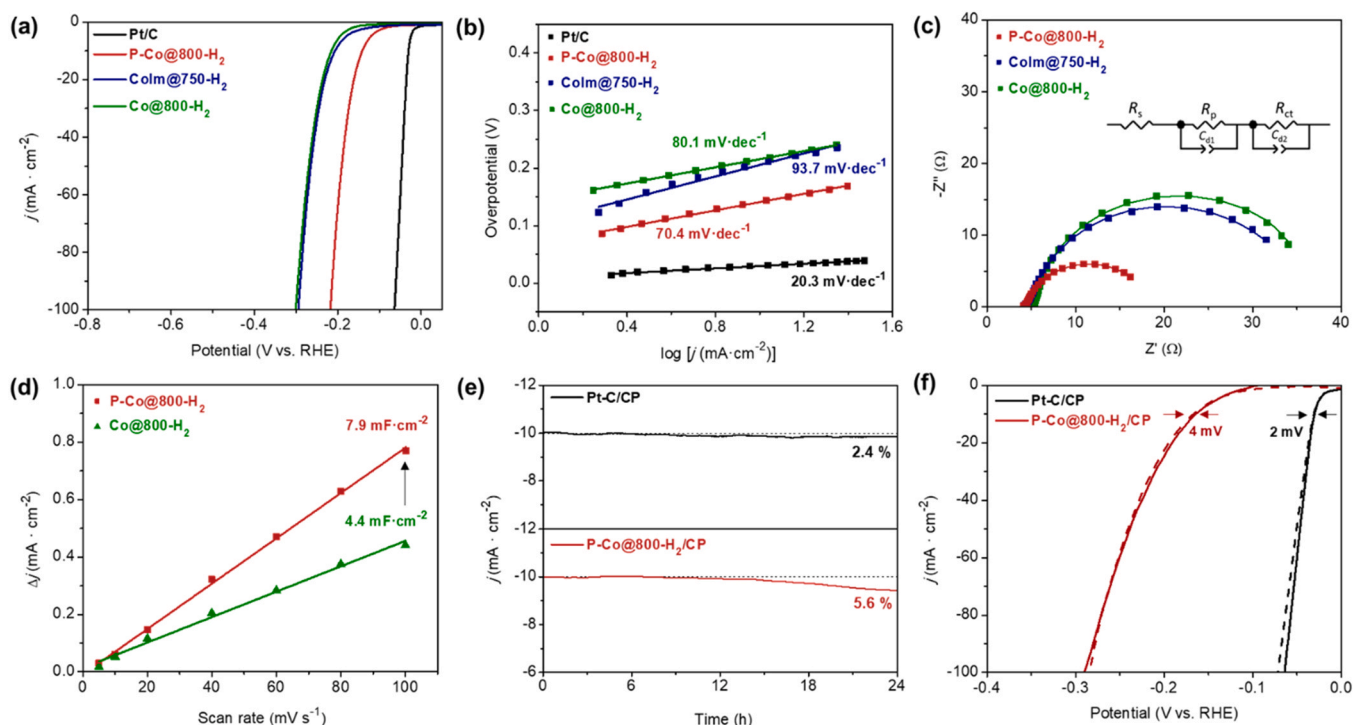


Fig. 6. HER evaluation of selected electrocatalysts in 0.5 M H_2SO_4 : (a) LSV curves; (b) Tafel plots; (c) EIS spectra at 180 mV (inset shows the equivalent impedance circuit model); (d) electrochemical double layer capacitances at 0.05 V; (e) long-term CA response of selected catalysts and (f) LSV curves before (straight line) and after (dashed line) CA stability tests (arrows indicate the overpotential variation).

and Fig. S24), which agrees with a decrease in particle size as confirmed by TEM analysis.

Moreover, the relatively high activity of **P-Co@800-H₂** for HER is accompanied by a remarkable stability for 24 h with low decays of current densities, 5.4 % (Fig. 6e). Consistent with the CA results (Fig. 6f), the LSV curve remain steadily after CA test. Furthermore, d-PDF analysis

and XPS analysis (Fig. S25 and Table S7) indicate that this catalyst is chemically stable in HER operating conditions, although a certain nanoparticle agglomeration seems to occur upon conducting HER tests, as revealed by TEM (Fig. S26). For some representative cases, we have constated that phosphide-based electrocatalysts systematically exhibit better HER performance than the metal pyrophosphate-based ones,

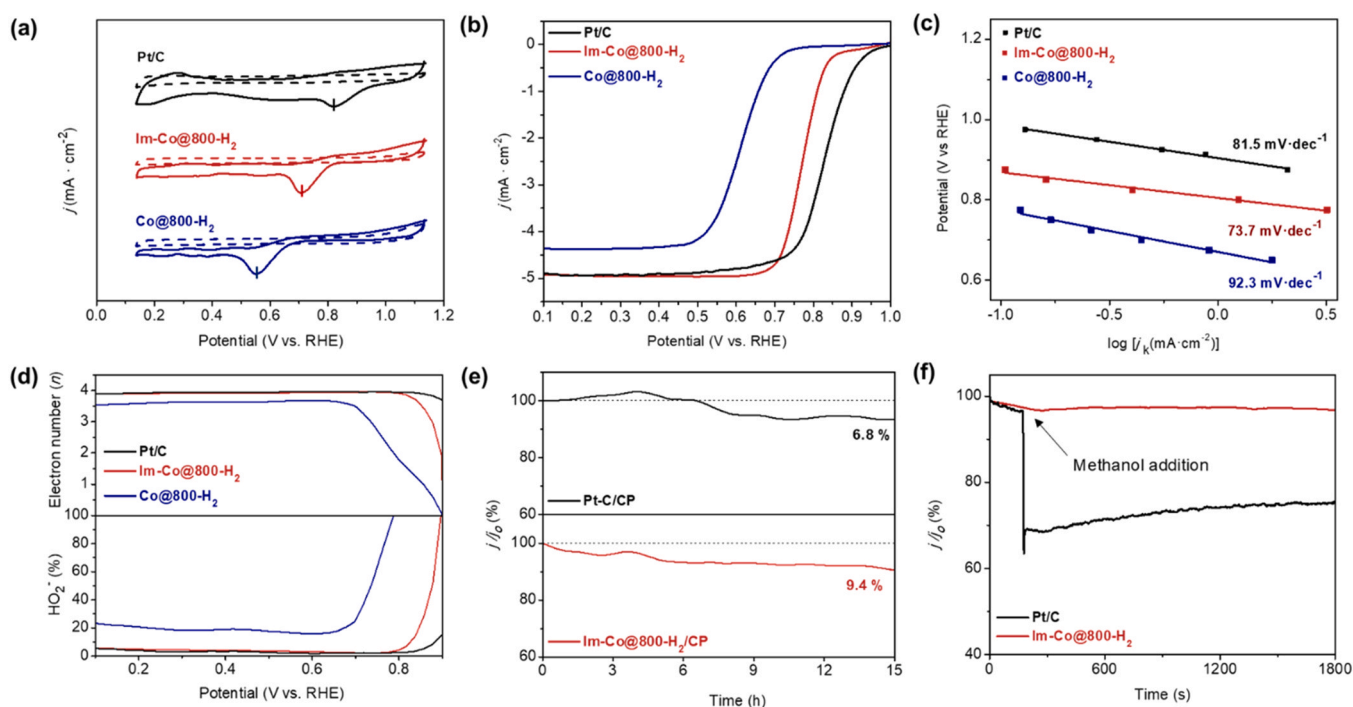


Fig. 7. ORR evaluation of the selected catalysts in 0.1 M KOH : (a) CV curves in O_2 (line) and N_2 (dashed lines)-saturated electrolyte; (b) LSV curves; (c) Tafel plots; (d) HO_2^- yield and the corresponding electron-transfer number; (e) long-term CA measurement at 0.5 V; and (f) CA responses on addition of methanol.

which may be ascribed to the presence of low valence metal centers (M^0/M^+) in the former materials [84].

3.3.3. Oxygen reduction reaction

LSV curves (Fig. S27) reveal that H_2 -pyrolysis is more effective than N_2 -pyrolysis to improve the ORR activity of the catalysts in terms of onset (E_{onset}) and half-wave potential ($E_{1/2}$) values (Tables S4 and S6). In addition, incorporating a second metal or an additional source of phosphorus (as PAA) has no significant effect on the ORR performance. In contrast, the effect of N-doping of the carbonaceous substrate was found as the most relevant factor to improve the performance, regardless of whether imidazole was physically mixed with the precursor prior to pyrolysis or used as a SAL upon synthesis (Figs. S28). Moreover, no appreciable changes in activity were observed by modifying the Im / CoHPA molar ratio in the range of 0.5–2 because both N-content and the pyrrolic / pyridinic ratio remains practically invariable, as determined by elemental analysis (Fig. S29 and Table S6) and XPS (Fig. S11).

Co@ 800- H_2 and the corresponding N-doped derivative, Im-Co@ 800- H_2 , were selected as representative electrocatalysts to study more in depth the ORR properties. Displacements to higher potential values of the oxygen reduction peak, only occurring in O_2 -saturated electrolyte (Fig. 7a), reveal a significantly improvement of the ORR performance for the N-doped catalyst relative to its counterpart. The former exhibits an oxygen reduction peak at ~ 0.78 V, slightly lower than that of Pt/C benchmark catalyst (0.84 V). As compared with Co@ 800- H_2 , the N-containing catalyst displays not only a remarkable increase in the E_{onset} and $E_{1/2}$ values, but also in the limiting current density ($j_{lim} \sim -5 \text{ mA} \cdot \text{cm}^{-2}$) (Fig. 7b). Moreover, Im-Co@ 800- H_2 presents a reaction kinetics slightly better than that of Pt/C benchmark catalyst (Figs. 7c and S30).

RRDE measurements were used for determining the number of electrons transfer per oxygen molecule (n). Based on RRDE tests, the calculated n values for the selected catalysts showed a considerable variation together with the HO_2^- yield in the potential region 0.2–0.8 V (Fig. 7d). In the case of Co@ 800- H_2 , n was around 3.5 and a HO_2^- yield of ~ 20 %. It is also worth noting that Im-Co@ 800- H_2 exhibits similar values to that of Pt/C benchmark catalyst ($n = 4$, HO_2^- yield ~ 5 %). In summary, the results obtained for Im-Co@ 800- H_2 reveals not only a high intrinsic activity, but also a favorable reaction kinetics in alkaline media.

The durability of Im-Co@ 800- H_2 after 15 h was confirmed by CA measurements (Fig. 7e), with a current decay about 9.4 %, nearby to that of the Pt/C catalyst (6.8 %). In contrast to that observed for Pt/C catalyst, CA tests for Im-Co@ 800- H_2 conducted after adding methanol to KOH electrolyte displayed the absence of oscillations in the current density (Fig. 7f), which is indicative of a strong methanol tolerance and superior ORR selectivity, desirable for application to direct methanol and/or alkaline fuel cells [89]. As illustrated for Im-Co@ 800- H_2 /CP,

post-reaction d-PDF analysis showed that no conversion into Co(OH) occurs in this case, but an enrichment in the o-CoP phase at the expense of the o-Co₂P phase took place (Fig. S31 and Table S7), although the coverage of cobalt phosphide particles by a layer of oxidized phosphate makes not evident the presence of these particles, as revealed by XPS data. Similarly, to that observed for HER tests, nanoparticle agglomeration also occurred upon conducting ORR tests (Fig. S32).

3.4. Alkaline water splitting

Several experiments intended to test the capability of the prepared catalysts as anode for overall water splitting in 1.0 M KOH solution have been conducted in a homemade assembled alkaline water electrolyzer (Fig. S33).

The P-Fe_{0.2}Co_{0.8}@ 800- H_2 (+)|20 %Pt/C(-) and Fe_{0.2}Co_{0.8}@ 500- N_2 (+)|20 %Pt/C(-) couples showed cell voltages of 1.58 V (at $10 \text{ mA} \cdot \text{cm}^{-2}$), which are comparable to that displayed by the RuO₂(+)|20%Pt/C(-) (1.59 V) couple (Fig. 8a). On applying a voltage of 1.58 V for 24 h (Fig. 8b), the observed decays for P-Fe_{0.2}Co_{0.8}@ 800- H_2 (+)|20 %Pt/C(-) and Fe_{0.2}Co_{0.8}@ 500- N_2 (+)|20 %Pt/C(-) couples were in the range of 12.1–15.6 %, similar to that of the RuO₂(+)|20 %Pt/C(-) couple (13.7 %). While current densities at low potentials were similar for the three tested cells, on applying higher potentials the systems P-Fe_{0.2}Co_{0.8}@ 800- H_2 (+)|20 %Pt/C(-) and Fe_{0.2}Co_{0.8}@ 500- N_2 (+)|20 %Pt/C(-) achieved lower decays than the commercial couple RuO₂(+)|20 %Pt/C(-) even generating higher current densities (Fig. S34). Interestingly, for higher current densities, the cell voltage required was even lower for the non-noble metal anode systems when compared with the noble metal benchmark couple. These results confirm the high OER activity of Fe-doped cobalt catalysts, showing performances better than the expensive RuO₂ commercial catalyst. Moreover, the produced amounts of hydrogen and oxygen gases are in good agreement with the theoretical values (Fig. 8c), giving rise to a Faraday efficiency close to 95 % after 70 min of operation. Thus, these results indicate superior durability and capability toward alkaline water splitting devices for the former electrode couples. XPS and TEM analysis for Fe_{0.2}Co_{0.8}@ 500- N_2 and P-Fe_{0.2}Co_{0.8}@ 800- H_2 after water splitting are shown in Figs. S35 and S36, respectively. As observed in the Co 2p_{3/2} and P 2p spectra no appreciable shifts of the binding energies are observed for none of the tested electrocatalysts. In both cases, a residual phosphorous content is still detected suggesting that oxidized phosphorous species are strongly adsorbed on the catalyst surfaces. Regarding the morphology, iron-containing cobalt (oxy)hydroxide nanoparticles appear clearly agglomerate after water splitting tests (Fig. S36).

4. Conclusions

From metal phosphonate derivatives $Fe_xCo_{1-x}[HO_3PCH(OH)CO_2] \cdot$

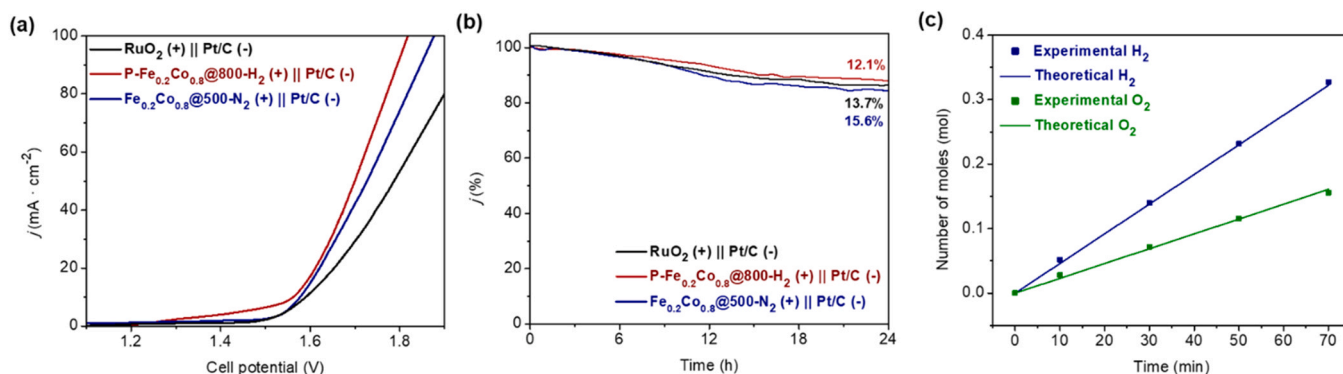


Fig. 8. (a) Polarization curves; (b) CA response, at a cell potential of 1.58 V for various electrodes couples in 1.0 M KOH; (c) Number of moles of generated gas, experimental and theoretical, for the couple P-Fe_{0.2}Co_{0.8}@ 800- H_2 (+)|20 %Pt/C(-).

2 H₂O, a variety of pyrophosphate- and phosphide-based Fe/Co electrocatalysts have been prepared. Modulation of the electrochemical properties has been further implemented by N-doping and control of the phases present in the electrocatalysts with additional phosphorus sources. A follow-up of the stability and chemical evolution of the electrocatalysts was carried out by synchrotron PDF analysis. In OER operating conditions, all pyrolyzed materials transformed into Fe/Co (oxy)hydroxides, composed of a mixture of small clusters (size ≤ 20 Å in diameter) derived from the polymorphs *P6₃/mmc* and *R-3m*. The best electrocatalytic performance for OER was obtained for the carbon paper-supported P-enriched solid solution, **P-Fe_{0.2}Co_{0.8}@ 800-H₂/CP**, with $\eta_{10} = 270$ mV and a phase composition of *o*-CoP (83.7 wt%) and *o*-Co₂P (16.3 wt%). In contrast, the same Fe/Co composition in the form of pyrophosphate, **Fe_{0.2}Co_{0.8}@ 500-N₂/CP**, provided a slightly higher overpotential (279 mV), which is attributed to the formation of subnanosize clusters of Fe-doped Co(OH) in both cases. Moreover, P-enriched cobalt phosphide displayed a remarkable HER activity in acidic conditions ($\eta_{10} = 140$ mV). N-doping in the surrounding carbonaceous support was found as the most simple and efficient strategy to improve the ORR performance for cobalt electrocatalysts, for which the reduction occurred via a four-electron mechanism. Lastly, we emphasize that both, amorphous Fe_{0.2}Co_{0.8} pyrophosphate and crystalline phosphide electrocatalysts, used as anode in an alkaline water splitting system, showed a cell voltage (1.58 V at 10 mA·cm⁻²) comparable to that of the noble metal-based benchmark system RuO₂(+)|20 %Pt/C(-) (1.59 V) and exhibited a similar stability for 24 h. Moreover, the cell voltage required at high current densities was even lower for the non-noble metal anode systems, when compared with the noble metal benchmark couple.

CRediT authorship contribution statement

Álvaro Vílchez-Cózar: Methodology, Investigation, Data curation, Writing – original draft. **Rosario M.P. Colodrero:** Investigation, Data curation, Writing – original draft, Supervision. **Montse Bazaga-García:** Investigation, Data curation. **David Marrero-López:** Conceptualization, Writing – review & editing. **Sayed M. El-refaie:** Writing – review & editing. **Patrícia A. Russo:** Writing – review & editing. **Nicola Pinna:** Writing – review & editing. **Pascual Olivera-Pastor:** Conceptualization, Writing – review & editing. **Aurelio Cabeza:** Conceptualization, Funding acquisition, Writing – review & editing, Supervision.

Declaration of Competing Interest

The authors declare that they have no known competing financial interests or personal relationships that could have appeared to influence the work reported in this paper.

Data availability

Data will be made available on request.

Acknowledgements

This work was funded by the PID2019-110249RB-I00/AEI/10.13039/501100011033; TED2021-129836B-I00/AEI/10.13039/501100011033/Unión Europea NextGenerationEU/PRTR (MICIU, Spain) and P20-00416 (Junta de Andalucía, Spain/FEDER) research projects. Synchrotron X-ray powder diffraction studies were performed at MSPD04 beamline at ALBA Synchrotron Light with the collaboration of ALBA staff. A.V.C. thanks MICIU for PRE2020-094459 student grant. R.M.P.C. acknowledges funding by project acknowledges B1_2022-23 (Plan Propio UMA). M.B.G. thanks PAIDI2020-DOC_00272 research grant (Junta de Andalucía, Spain). Funding for open access charge: Universidad de Málaga / CBUA.

Appendix A. Supporting information

Supplementary data associated with this article can be found in the online version at doi:10.1016/j.apcatb.2023.122963.

References

- [1] C. Li, J.-B. Baek, Recent advances in noble metal (Pt, Ru, and Ir)-based electrocatalysts for efficient hydrogen evolution reaction, *ACS Omega* 5 (2020) 31–40, <https://doi.org/10.1021/acsomega.9b03550>.
- [2] J. Wang, F. Xu, H. Jin, Y. Chen, Y. Wang, Non-noble metal-based carbon composites in hydrogen evolution reaction: fundamentals to applications, *Adv. Mater.* 29 (2017), 1605838, <https://doi.org/10.1002/adma.201605838>.
- [3] X. Li, J. Wang, Phosphorus-based electrocatalysts: black phosphorus, metal phosphides and phosphates, *Adv. Mater. Interfaces* 7 (2020), 2000676, <https://doi.org/10.1002/admi.202000676>.
- [4] Z. Pu, T. Liu, I.S. Amiin, R. Cheng, P. Wang, C. Zhang, P. Ji, W. Hu, J. Liu, S. Mu, Transition-metal phosphides: activity origin, energy-related electrocatalysis applications, and synthetic strategies, *Adv. Funct. Mater.* 30 (2020), 2004009, <https://doi.org/10.1002/adfm.202004009>.
- [5] P. Bhanja, J. Na, T. Jing, J. Lin, T. Wakihara, A. Bhaumik, Y. Yamauchi, Nanoarchitected metal phosphates and phosphonates: a new material horizon toward emerging applications, *Chem. Mater.* 31 (2019) 5343–5362, <https://doi.org/10.1021/acs.chemmater.9b01742>.
- [6] X.-W. Lv, C.-C. Weng, Y.-P. Zhu, Z.-Y. Yuan, Nanoporous metal phosphonate hybrid materials as a novel platform for emerging applications: a critical review, *Small* 17 (2021), 2005304, <https://doi.org/10.1002/sml.202005304>.
- [7] H. Zhao, Z.-Y. Yuan, Design Strategies of transition-metal phosphate and phosphonate electrocatalysts for energy-related reactions, *ChemSusChem* 14 (2021) 130–149, <https://doi.org/10.1002/cssc.202002103>.
- [8] Q. Ren, H. Wang, X.-F. Lu, Y.-X. Tong, G.-R. Li, Recent progress on MOF-derived heteroatom-doped carbon-based electrocatalysts for oxygen reduction reaction, *Adv. Sci.* 5 (2018), 1700515, <https://doi.org/10.1002/adv.201700515>.
- [9] Y.-P. Zhu, Z.-Y. Yuan, H.N. Alshareef, New opportunities for functional materials from metal phosphonates, *ACS Mater. Lett.* 2 (2020) 582–594, <https://doi.org/10.1021/acsmaterialslett.0c00095>.
- [10] Y. Li, Z. Dong, L. Jiao, Multifunctional transition metal-based phosphides in energy-related electrocatalysis, *Adv. Energy Mater.* 10 (2020), 1902104, <https://doi.org/10.1002/aenm.201902104>.
- [11] W. Zhang, N. Han, J. Luo, X. Han, S. Feng, W. Guo, S. Xie, Z. Zhou, P. Subramanian, K. Wan, J. Arbiol, C. Zhang, S. Liu, M. Xu, X. Zhang, J. Fransaer, Critical role of phosphorus in hollow structures cobalt-based phosphides as bifunctional catalysts for water splitting, *Small* 18 (2022), 2103561, <https://doi.org/10.1002/sml.202103561>.
- [12] J. Wang, Z. Liu, Y. Zheng, L. Cui, W. Yang, J. Liu, Recent advances in cobalt phosphide based materials for energy-related applications, *J. Mater. Chem. A* 5 (2017) 22913–22932, <https://doi.org/10.1039/C7TA08386F>.
- [13] C. Lin, P. Wang, H. Jin, J. Zhao, D. Chen, S. Liu, C. Zhang, S. Mu, An iron-doped cobalt phosphide nano-electrocatalyst derived from a metal-organic framework for efficient water splitting, *Dalton Trans.* 48 (2019) 16555–16561, <https://doi.org/10.1039/C9DT03619A>.
- [14] C. Yang, T. He, W. Zhou, R. Deng, Q. Zhang, Iron-tuned 3D cobalt–phosphate catalysts for efficient hydrogen and oxygen evolution reactions over a wide pH range, *ACS Sustain. Chem. Eng.* 8 (2020) 13793–13804, <https://doi.org/10.1021/acssuschemeng.0c04966>.
- [15] L. Xiong, B. Wang, H. Cai, H. Hao, J. Li, T. Yang, S. Yang, Understanding the doping effect on hydrogen evolution activity of transition-metal phosphides: modeled with Ni₂P, *Appl. Catal. B* 295 (2021), 120283, <https://doi.org/10.1016/j.apcatb.2021.120283>.
- [16] Y. Kang, S. Wang, S. Zhu, H. Gao, K.S. Hui, C.-Z. Yuan, H. Yin, F. Bin, X.-L. Wu, W. Mai, L. Zhu, M. Hu, F. Liang, F. Chen, K.N. Hui, Iron-modulated nickel cobalt phosphide embedded in carbon to boost power density of hybrid sodium–air battery, *Appl. Catal. B* 285 (2021), 119786, <https://doi.org/10.1016/j.apcatb.2020.119786>.
- [17] S. Wang, P. Yang, X. Sun, H. Xing, J. Hu, P. Chen, Z. Cui, W. Zhu, Z. Ma, Synthesis of 3D heterostructure Co-doped Fe₂P electrocatalyst for overall seawater electrolysis, *Appl. Catal. B* 297 (2021), 120386, <https://doi.org/10.1016/j.apcatb.2021.120386>.
- [18] X. Zhang, A. Wu, D. Wang, Y. Jiao, H. Yan, C. Jin, Y. Xie, C. Tian, Fine-tune the electronic structure in Co-Mo based catalysts to give easily coupled HER and OER catalysts for effective water splitting, *Appl. Catal. B* 328 (2023), 122474, <https://doi.org/10.1016/j.apcatb.2023.122474>.
- [19] X. Zhang, D. Kim, X. Guo, Y. Zhu, L.Y.S. Lee, Impacts of boron doping on the atomic structure, stability, and photocatalytic activity of Cu₃P nanocrystals, *Appl. Catal. B* 298 (2021), 120515, <https://doi.org/10.1016/j.apcatb.2021.120515>.
- [20] X.-W. Lv, W.-S. Xu, W.-W. Tian, H.-Y. Wang, Z.-Y. Yuan, Activity promotion of core and shell in multifunctional core-shell Co₂P@NC electrocatalyst by secondary metal doping for water electrolysis and Zn-air batteries, *Small* 17 (2021), 2101856, <https://doi.org/10.1002/sml.202101856>.
- [21] M.M. Kumar, C.R. Raj, Heteroatom-doped carbon-encapsulated FeP nanostructure: a multifunctional electrocatalyst for zinc-air battery and water electrolyzer, *ACS Appl. Mater. Interfaces* 14 (2022) 15176–15186, <https://doi.org/10.1021/acsami.1c24918>.

- [22] M. Chen, J. Liu, X.-Q. Wang, L.-L. Shao, Z.-Y. Yuan, X. Qian, Y.-N. Wang, A.-X. Ding, Y.-S. Tian, Ultrafine transition metal phosphide nanoparticles semiembedded in nitrogen-doped carbon nanotubes for efficient counter electrode materials in dye-sensitized solar cells, *ACS Appl. Energy Mater.* 4 (2021) 13952–13962, <https://doi.org/10.1021/acs.aem.1c02765>.
- [23] D. Xue, F. Yu, Q. Ying, Y. Wu, W.-J. Lee, S.-H. Kwon, Y. Yang, Phosphate-assisted dispersion of iron phosphide in carbon nanosheets towards efficient and durable ORR catalysts in acidic and alkaline media, *ChemCatChem* 13 (2021) 4431–4441, <https://doi.org/10.1002/cctc.202100947>.
- [24] L. Hu, Y. Hu, R. Liu, Y. Mao, M.-S. (J. Tang) Balogun, Y. Tong, Co-based MOF-derived Co/CoN/Co₂P ternary composite embedded in N- and P-doped carbon as bifunctional nanocatalysts for efficient overall water splitting, *Int. J. Hydrog. Energy* 44 (2019) 11402–11410, <https://doi.org/10.1016/j.ijhydene.2019.03.157>.
- [25] T. Zhou, Y. Du, D. Wang, S. Yin, W. Tu, Z. Chen, A. Borgna, R. Xu, Phosphonate-based metal-organic framework derived Co-P-C hybrid as an efficient electrocatalyst for oxygen evolution reaction, *ACS Catal.* 7 (2017) 6000–6007, <https://doi.org/10.1021/acscatal.7b00937>.
- [26] H. Zhao, Z.-Y. Yuan, Insights into transition metal phosphate materials for efficient electrocatalysis, *ChemCatChem* 12 (2020) 3797–3810, <https://doi.org/10.1002/cctc.202000360>.
- [27] L. Song, T. Zheng, L. Zheng, B. Lu, H. Chen, Q. He, W. Zheng, Y. Hou, J. Lian, Y. Wu, J. Chen, Z. Ye, J. Lu, Cobalt-doped basic iron phosphate as bifunctional electrocatalyst for long-life and high-power-density rechargeable zinc-air batteries, *Appl. Catal. B* 300 (2022), 120712, <https://doi.org/10.1016/j.apcatb.2021.120712>.
- [28] C.-J. Huang, H.-M. Xu, T.-Y. Shuai, Q.-N. Zhan, Z.-J. Zhang, G.-R. Li, A review of modulation strategies for improving catalytic performance of transition metal phosphides for oxygen evolution reaction, *Appl. Catal. B* 325 (2023), 122313, <https://doi.org/10.1016/j.apcatb.2022.122313>.
- [29] R. Li, D. Wang, Understanding the structure-performance relationship of active sites at atomic scale, *Nano Res.* 15 (2022) 6888–6923, <https://doi.org/10.1007/s12274-022-4371-x>.
- [30] Y. Huang, L. Hu, R. Liu, Y. Hu, T. Xiong, W. Qiu, M.-S. (J. Tang) Balogun, A. Pan, Y. Tong, Nitrogen treatment generates tunable nanohybridization of Ni₃P₄ nanosheets with nickel hydr(oxy)oxides for efficient hydrogen production in alkaline, seawater and acidic media, *Appl. Catal. B* 251 (2019) 181–194, <https://doi.org/10.1016/j.apcatb.2019.03.037>.
- [31] Y. Yan, K. Huang, J. Lin, T. Yang, P. Wang, L. Qiao, W. Cai, X. Zheng, Charge redistribution in FeOOH nanorod array by ecological oxygen-reduction deposition for boosting electrocatalytic water oxidation, *Appl. Catal. B* 330 (2023), 122595, <https://doi.org/10.1016/j.apcatb.2023.122595>.
- [32] J. Liu, X. Liu, H. Shi, J. Luo, L. Wang, J. Liang, S. Li, L.-M. Yang, T. Wang, Y. Huang, Q. Li, Breaking the scaling relations of oxygen evolution reaction on amorphous NiFeP nanostructures with enhanced activity for overall seawater splitting, *Appl. Catal. B* 302 (2022), 120862, <https://doi.org/10.1016/j.apcatb.2021.120862>.
- [33] F. Yang, T. Xiong, P. Huang, S. Zhou, Q. Tan, H. Yang, Y. Huang, M.-S. (J. Tang) Balogun, Nanostructured transition metal compounds coated 3D porous core-shell carbon fiber as monolith water splitting electrocatalysts: a general strategy, *Chem. Eng. J.* 423 (2021), 130279, <https://doi.org/10.1016/j.cej.2021.130279>.
- [34] C. Lyu, J. Cheng, K. Wu, J. Wu, N. Wang, Z. Guo, P. Hu, W.-M. Lau, J. Zheng, Interfacial electronic structure modulation of CoP nanowires with FeP nanosheets for enhanced hydrogen evolution under alkaline water/seawater electrolytes, *Appl. Catal. B* 317 (2022), 121799, <https://doi.org/10.1016/j.apcatb.2022.121799>.
- [35] M. Jin, X. Zhang, R. Shi, Q. Lian, S. Niu, O. Peng, Q. Wang, C. Cheng, Hierarchical CoP@Ni₂P catalysts for pH-universal hydrogen evolution at high current density, *Appl. Catal. B* 296 (2021), 120350, <https://doi.org/10.1016/j.apcatb.2021.120350>.
- [36] V.H. Hoa, M. Austeria, H.T. Dao, M. Mai, D.H. Kim, Dual-phase cobalt phosphide/phosphate hybrid interactions via iridium nanocluster interfacial engineering toward efficient overall seawater splitting, *Appl. Catal. B* 327 (2023), 122467, <https://doi.org/10.1016/j.apcatb.2023.122467>.
- [37] X. Wang, H. Huang, J. Qian, Y. Li, K. Shen, Intensified Kirkendall effect assisted construction of double-shell hollow Cu-doped CoP nanoparticles anchored by carbon arrays for water splitting, *Appl. Catal. B* 325 (2023), 122295, <https://doi.org/10.1016/j.apcatb.2022.122295>.
- [38] X. Hu, R. Wang, W. Feng, C. Xu, Z. Wei, Electrocatalytic oxygen evolution activities of metal chalcogenides and phosphides: fundamentals, origins, and future strategies, *J. Energy Chem.* 81 (2023) 167–191, <https://doi.org/10.1016/j.ijechem.2023.01.062>.
- [39] D.F.S. Gallis, H.D. Pratt III, T.M. Anderson, K.W. Chapman, Electrochemical activity of Fe-MIL-100 as a positive electrode for Na-ion batteries, *J. Mater. Chem. A* 4 (2016) 13764–13770, <https://doi.org/10.1039/C6TA03943J>.
- [40] K. Xiang, W. Xing, D.B. Ravnsbæk, L. Hong, M. Tang, Z. Li, K.M. Wiaderek, O. J. Borkiewicz, K.W. Chapman, P.J. Chupas, Accommodating high transformation strains in battery electrodes via the formation of nanoscale intermediate phases: operando investigation of olivine NaFePO₄, *Nano Lett.* 17 (2017) 1696–1702, <https://doi.org/10.1021/acs.nanolett.6b04971>.
- [41] Y. Li, Q. An, Y. Cheng, Y. Liang, Y. Ren, C.-J. Sun, H. Dong, Z. Tang, G. Li, Y. Yao, A high-voltage rechargeable magnesium-sodium hybrid battery, *Nano Energy* 34 (2017) 188–194, <https://doi.org/10.1016/j.nanoen.2017.02.012>.
- [42] M. Moriya, M. Miyahara, M. Hokazono, H. Sasaki, A. Nemoto, S. Katayama, Y. Akimoto, S.-i. Hirano, Y. Ren, High-energy X-ray powder diffraction and atomic-pair distribution-function studies of charged/discharged structures in carbon-hybridized Li₂MnSiO₄ nanoparticles as a cathode material for lithium-ion batteries, *J. Power Sources* 263 (2014) 7–12, <https://doi.org/10.1016/j.jpowsour.2014.03.065>.
- [43] M.W. Terban, S.J.L. Billinge, Structural analysis of molecular materials using the pair distribution function, *Chem. Rev.* 122 (2022) 1208–1272, <https://doi.org/10.1021/acs.chemrev.1c00237>.
- [44] C.L. Farrow, D. Kwabena Bediako, Y. Surendranath, D.G. Nocera, S.J.L. Billinge, Intermediate-range structure of self-assembled cobalt-based oxygen-evolving catalyst, *J. Am. Chem. Soc.* 135 (2013) 6403–6406, <https://doi.org/10.1021/ja401276f>.
- [45] H. Zhu, Y. Huang, J. Ren, B. Zhang, Y. Ke, A.K.-Y. Jen, Q. Zhang, X.-L. Wang, Q. Li, Bridging structural inhomogeneity to functionality: pair distribution function methods for functional materials development, *Adv. Sci.* 8 (2021), 2003534, <https://doi.org/10.1002/advs.202003534>.
- [46] W. Li, R. Harrington, Y. Tang, J.D. Kubicki, M. Aryanpour, R.J. Reeder, J.B. Parise, B.L. Phillips, Differential pair distribution function study of the structure of arsenate adsorbed on nanocrystalline γ -alumina, *Environ. Sci. Technol.* 45 (2011) 9687–9692, <https://doi.org/10.1021/es200750b>.
- [47] S. Shiotani, K. Ohara, H. Tsukasaki, S. Mori, R. Kanno, Pair distribution function analysis of sulfide glassy electrolytes for all-solid-state batteries: understanding the improvement of ionic conductivity under annealing condition, *Sci. Rep.* 7 (2017) 6972, <https://doi.org/10.1038/s41598-017-07086-y>.
- [48] J. Peterson, J. TenCate, Th Proffen, T. Darling, H. Nakotte, K. Page, Quantifying amorphous and crystalline phase content with the atomic pair distribution function, *J. Appl. Cryst.* 46 (2013) 332–336, <https://doi.org/10.1107/S0021889812050595>.
- [49] R. Harrington, D.B. Hausner, N. Bhandari, D.R. Strongin, K.W. Chapman, P. J. Chupas, D.S. Middlemiss, C.P. Grey, J.B. Parise, Investigation of surface structures by powder diffraction: a differential pair distribution function study on arsenate sorption on ferrihydrite, *Inorg. Chem.* 49 (2010) 325–330, <https://doi.org/10.1021/ic9022695>.
- [50] R. Sgarbi, K. Kumar, V.A. Saveleva, L. Dubau, R. Chattot, V. Martin, M. Mermoux, P. Bordet, P. Glatzel, E.A. Ticianelli, F. Jaouen, F. Maillard, Electrochemical transformation of Fe-N-C catalysts into iron oxides in alkaline medium and its impact on the oxygen reduction reaction activity, *Appl. Catal. B* 311 (2022), 121366, <https://doi.org/10.1016/j.apcatb.2022.121366>.
- [51] A.G. De La Torre, S. Bruque, M.A.G. Aranda, Rietveld quantitative amorphous content analysis, *J. Appl. Crystallogr.* 34 (2001) 196–202, <https://doi.org/10.1107/S0021889801002485>.
- [52] M. Bazaga-García, Á. Vilchez-Cózar, B. Maranescu, P. Olivera-Pastor, M. Marganovici, G. Ilia, A. Cabeza, A. Visa, R.M.P. Colodrero, Synthesis and electrochemical properties of metal(II)-carboxyethylphenylphosphinates, *Dalton Trans.* 50 (2021) 6539–6548, <https://doi.org/10.1039/D1DT00104C>.
- [53] A. Altomare, C. Cuocci, C. Giacovazzo, A. Moliterni, R. Rizzi, N. Corriero, A. Falcichio, EXPO2013: a kit of tools for phasing crystal structures from powder data, *J. Appl. Crystallogr.* 46 (2013) 1231–1235, <https://doi.org/10.1107/S0021889813013113>.
- [54] H.M. Rietveld, A profile refinement method for nuclear and magnetic structures, *J. Appl. Crystallogr.* 2 (1969) 65–71, <https://doi.org/10.1107/S0021889869006558>.
- [55] B.H. Toby, R.B. Von Dreele, GSAS-II: the genesis of a modern open-source all purpose crystallography software package, *J. Appl. Crystallogr.* 46 (2013) 544–549, <https://doi.org/10.1107/S0021889813003531>.
- [56] P. Juhás, T. Davis, C.L. Farrow, S.J.L. Billinge, PDFgetX3: a rapid and highly automatable program for processing powder diffraction data into total scattering pair distribution functions, *J. Appl. Cryst.* 46 (2013) 560–566, <https://doi.org/10.1107/S0021889813005190>.
- [57] C.L. Farrow, P. Juhás, J.W. Liu, D. Bryndin, E.S. Božin, J. Bloch, T. Proffen, S. J. Billinge, PDFfit2 and PDFgui: computer programs for studying nanostructure in crystals, *J. Phys. Condens. Mater.* 19 (2007), 335219, <https://doi.org/10.1088/0953-8984/19/33/335219>.
- [58] I.-K. Jeong, T. Proffen, F. Mohiuddin-Jacobs, S.J.L. Billinge, Measuring correlated atomic motion using X-ray diffraction, *J. Phys. Chem. A* 103 (1999) 921–924, <https://doi.org/10.1021/JP9836978>.
- [59] I.-K. Jeong, R.H. Heffner, M.J. Graf, S.J.L. Billinge, Lattice dynamics and correlated atomic motion from the atomic pair distribution function, *Phys. Rev. B* 67 (2003), 104301, <https://doi.org/10.1103/PhysRevB.67.104301>.
- [60] C. Wei, R.R. Rao, J. Peng, B. Huang, I.E.L. Stephens, M. Risch, Z.J. Xu, Y. Shao-Hor, Recommended practices and benchmark activity for hydrogen and oxygen electrocatalysis in water splitting and fuel cells, *Adv. Mater.* 31 (2019), 1806296, <https://doi.org/10.1002/adma.201806296>.
- [61] C.C.L. McCrory, S. Jung, I.M. Ferrer, S.M. Chatman, J.C. Peters, T.F. Jaramillo, Benchmarking hydrogen evolving reaction and oxygen evolving reaction electrocatalysts for solar water splitting devices, *J. Am. Chem. Soc.* 137 (2015) 4347–4357, <https://doi.org/10.1021/ja510442p>.
- [62] C.C.L. McCrory, S. Jung, J.C. Peters, T.F. Jaramillo, Benchmarking heterogeneous electrocatalysts for the oxygen evolution reaction, *J. Am. Chem. Soc.* 135 (2013) 16977–16987, <https://doi.org/10.1021/ja407115p>.
- [63] S. Gutiérrez-Tarriño, J.L. Olloqui-Sariego, J.J. Calvente, G. Mínguez Espallargas, F. Rey, A. Corma, P. Oña-Burgos, Cobalt metal-organic framework based on layered double nanosheets for enhanced electrocatalytic water oxidation in neutral media, *J. Am. Chem. Soc.* 142 (2020) 19198–19208, <https://doi.org/10.1021/jacs.0c08882>.
- [64] I.R. Salcedo, M. Bazaga-García, A. Cuesta, E.R. Losilla, K.D. Demadis, P. Olivera-Pastor, R.M.P. Colodrero, A. Cabeza, NH₃/H₂O-mediated proton conductivity and photocatalytic behaviour of Fe(II)-hydroxyphosphonoacetate and M(II)-substituted derivatives, *Dalton Trans.* 49 (2020) 3981–3988, <https://doi.org/10.1039/C9DT04210E>.

- [65] R. Fu, S. Xiang, H. Zhang, J. Zhang, X. Wu, Syntheses, characterization, and magnetic properties of four new layered transition-metal hydroxyl-carboxylate-phosphonates: $[M(\text{CH}(\text{OH})(\text{CO}_2)(\text{PO}_3\text{H}))(\text{H}_2\text{O})_2]$ ($M = \text{Mn, Fe, Co, Zn}$), Cryst. Growth Des. 5 (2005) 1795–1799, <https://doi.org/10.1021/cg050065j>.
- [66] J. Wang, T. Liao, Z. Wei, J. Sun, J. Guo, Z. Sun, Heteroatom-doping of non-noble metal-based catalysts for electrocatalytic hydrogen evolution: an electronic structure tuning strategy, Small Methods 5 (2021), 2000988, <https://doi.org/10.1002/smt.20200988>.
- [67] Z. Wu, L. Huang, H. Liu, M. Li, H. Wang, Surface oxidation of transition metal sulfide and phosphide nanomaterials, Nano Res 14 (2021) 2264–2267, <https://doi.org/10.1007/s12274-020-3219-5>.
- [68] D. Lai, Qi Kang, F. Gao, Q. Lu, High-entropy effect of a metal phosphide on enhanced overall water splitting performance, J. Mater. Chem. A 9 (2021) 17913–17922, <https://doi.org/10.1039/D1TA04755H>.
- [69] A.P. Grosvenor, S.D. Wik, R.G. Cavell, A. Mar, Examination of the bonding in binary transition-metal monophosphides MP ($M = \text{Cr, Mn, Fe, Co}$) by X-ray photoelectron spectroscopy, Inorg. Chem. 44 (2005) 8988–8998, <https://doi.org/10.1021/ic051004d>.
- [70] M. Jiang, J. Li, J. Li, Y. Zhao, L. Pan, Q. Cao, D. Wang, Y. Du, Two-dimensional bimetallic phosphide ultrathin nanosheets as non-noble electrocatalysts for a highly efficient oxygen evolution reaction, Nanoscale 11 (2019) 9654–9660, <https://doi.org/10.1039/C8NR10521A>.
- [71] Y. Li, Q. Liu, S. Zhang, G. Li, The vital balance of graphitization and defect engineering for efficient bifunctional oxygen electrocatalyst based on N-doping carbon/CNT frameworks, ChemCatChem 11 (2019) 861–867, <https://doi.org/10.1002/cctc.201801678>.
- [72] S. Ramakrishnan, D.B. Velusamy, S. Sengodan, G. Nagaraju, D.H. Kim, A.R. Kim, D. J. Yoo, Rational design of multifunctional electrocatalyst: an approach towards efficient overall water splitting and rechargeable flexible solid-state zinc-air battery, Appl. Catal. B 300 (2022), 120752, <https://doi.org/10.1016/j.apcatb.2021.120752>.
- [73] J. Hu, Y. Qin, H. Sun, Y. Ma, L. Lin, Y. Peng, J. Zhong, M. Chen, X. Zhao, Z. Deng, Combining multivariate electrospinning with surface MOF functionalization to construct tunable active sites toward trifunctional electrocatalysis, Small 18 (2022), 2106260, <https://doi.org/10.1002/sml.202106260>.
- [74] N.-T. Suen, S.-F. Hung, Q. Quan, N. Zhang, Y.-J. Xu, H.M. Chen, Electrocatalysis for the oxygen evolution reaction: recent development and future perspectives, Chem. Soc. Rev. 46 (2017) 337–365, <https://doi.org/10.1039/C6CS00328A>.
- [75] W.-F. Chen, C.-H. Wang, K. Sasaki, N. Marinkovic, W. Xu, J.T. Muckerman, Y. Zhu, R.R. Adzic, Highly active and durable nanostructured molybdenum carbide electrocatalysts for hydrogen production, Energy Environ. Sci. 6 (2013) 943–951, <https://doi.org/10.1039/C2EE23891H>.
- [76] P. Feng, X. Cheng, J. Li, X. Luo, $\text{Co}_3(\text{PO}_4)_2$ nanoparticles embedded in nitrogen-doped carbon as an advanced electrocatalyst for OER in alkaline solution, Catal. Lett. 148 (2018) 214–219, <https://doi.org/10.1007/s10562-017-2251-x>.
- [77] S.M. El-Refaei, P.A. Russo, P. Amsalem, N. Koch, N. Pinna, The importance of ligand selection on the formation of metal phosphonate-derived CoMoP and CoMoP₂ nanoparticles for catalytic hydrogen evolution, ACS Appl. Nano Mater. 3 (2020) 4147–4156, <https://doi.org/10.1021/acsanm.0c00319>.
- [78] S. Jung, C.C.L. McCrory, I.M. Ferrer, J.C. Peters, T.F. Jaramillo, Benchmarking nanoparticulate metal oxide electrocatalysts for the alkaline water oxidation reaction, J. Am. Chem. Soc. 138 (2016) 3068–3076, <https://doi.org/10.1039/C5TA07586F>.
- [79] T. Zhou, Z. Cao, P. Zhang, H. Ma, Z. Gao, H. Wang, Y. Lu, J. He, Y. Zhao, Transition metal ions regulated oxygen evolution reaction performance of Ni-based hydroxides hierarchical nanoarrays, Sci. Rep. 7 (2017) 46154, <https://doi.org/10.1038/srep46154>.
- [80] G. Kwon, H. Jang, J.-S. Lee, A. Mane, D.J. Mandia, S.R. Soltan, L.M. Utschig, A.B. F. Martinson, D.M. Tiede, H. Kim, J. Kim, Resolution of electronic and structural factors underlying oxygen-evolving performance in amorphous cobalt oxide catalysts, J. Am. Chem. Soc. 140 (2018) 10710–10720, <https://doi.org/10.1021/jacs.8b02719>.
- [81] L. Yang, P. Juhaš, M.W. Terban, M.G. Tuckerd, S.J.L. Billinge, Structure-mining: screening structure models by automated fitting to the atomic pair distribution function over large numbers of models, Acta Cryst. A76 (2020) 395–409, <https://doi.org/10.1107/S2053273320002028>.
- [82] X. Liu, Q. Yin, C. Dai, G. Li, J. Lian, Y. Zhao, S. Yang, H. Li, Amorphous bimetallic phosphate-carbon precatalyst with deep self-reconstruction toward efficient oxygen evolution reaction and Zn-air batteries, ACS Sustain. Chem. Eng. 9 (2021) 5345–5355, <https://doi.org/10.1021/acssuschemeng.0c09339>.
- [83] D. Friebe, M.W. Louie, M. Bajdich, K.E. Sanwald, Y. Cai, A.M. Wise, M.-J. Cheng, D. Sokaras, T.-C. Weng, R. Alonso-Mori, R.C. Davis, J.R. Bargar, J.K. Nørskov, A. Nilsson, A.T. Bell, Identification of highly active Fe sites in (Ni,Fe)OOH for electrocatalytic water splitting, J. Am. Chem. Soc. 137 (2015) 1305–1313, <https://doi.org/10.1021/ja511559d>.
- [84] Y. Zhao, N. Dongfang, C.A. Triana, C. Huang, R. Erni, W. Wan, J. Li, D. Stoian, L. Pan, P. Zhang, J. Lan, M. Iannuzzi, G.R. Patzke, Dynamics and control of active sites in hierarchically nanostructured cobalt phosphide/chalcogenide-based electrocatalysts for water splitting, Energy Environ. Sci. 15 (2022) 727–739, <https://doi.org/10.1039/D1EE02249K>.
- [85] Y. Pan, Y. Lin, Y. Chen, Y. Liu, C. Liu, Cobalt phosphide-based electrocatalysts: synthesis and phase catalytic activity comparison for hydrogen evolution, J. Mater. Chem. A 4 (2016) 4745–4754, <https://doi.org/10.1039/C6TA00575F>.
- [86] A. Vilchez-Cózar, E. Armakola, M. Gjika, A. Visa, M. Bazaga-García, P. Olivera-Pastor, D. Choquesillo-Lazarte, D. Marrero-López, A. Cabeza, R.M.P. Colodrero, K. D. Demadis, Exploiting the multifunctionality of M^{2+} /imidazole-etidronates for proton conductivity (Zn^{2+}) and electrocatalysis (Co^{2+} , Ni^{2+}) toward the HER, OER, and ORR, ACS Appl. Mater. Interfaces 14 (2022) 11273–11287, <https://doi.org/10.1021/acsami.1c21876>.
- [87] A. Ray, S. Sultana, L. Paramanik, K.M. Parida, Recent advances in phase, size, and morphology-oriented nanostructured nickel phosphide for overall water splitting, J. Mater. Chem. A 8 (2020) 19196–19245, <https://doi.org/10.1039/D0TA05797E>.
- [88] H. Wang, W. Fu, X. Yang, Z. Huang, J. Li, H. Zhang, Y. Wang, Recent advancements in heterostructured interface engineering for hydrogen evolution reaction electrocatalysis, J. Mater. Chem. A 8 (2020) 6926–6956, <https://doi.org/10.1039/C9TA11646J>.
- [89] H. Singh, M. Marley-Hines, S. Chakravarty, M. Nath, Multi-walled carbon nanotube supported manganese selenide as a highly active bifunctional OER and ORR electrocatalyst, J. Mater. Chem. A 10 (2022) 6772–6784, <https://doi.org/10.1039/D1TA09864K>.